



## Cavezzo—The double face of a meteorite: Mineralogy, petrography, and geochemistry of a very unusual chondrite

Giovanni PRATESI <sup>1,2\*</sup>, Vanni MOGGI CECCHI<sup>3</sup>, Richard C. GREENWOOD<sup>4</sup>, Ian A. FRANCHI<sup>4</sup>, Samantha J. HAMMOND<sup>4</sup>, Mario DI MARTINO<sup>5</sup>, Dario BARGHINI <sup>5,6</sup>, Carla TARICCO<sup>6</sup>, Albino CARBOGNANI<sup>7</sup>, and Daniele GARDIOL<sup>5</sup>

<sup>1</sup>Dipartimento di Scienze della Terra, Università degli Studi di Firenze, Via G. La Pira 4, Florence 50121, Italy

<sup>2</sup>INAF—Istituto di Astrofisica e Planetologia Spaziali, Via Fosso del Cavaliere 100, Rome 00133, Italy

<sup>3</sup>Museo di Storia Naturale, Università degli Studi di Firenze, Via G. La Pira 4, Florence 50121, Italy

<sup>4</sup>Planetary and Space Sciences, The Open University, Milton Keynes MK7 6AA, UK

<sup>5</sup>INAF—Osservatorio Astrofisico di Torino, Via Osservatorio 20, Turin 10025, Italy

<sup>6</sup>Dipartimento di Fisica, Università degli Studi di Torino, Via P. Giuria 1, Pino Torinese 10125, Italy

<sup>7</sup>INAF—Osservatorio di Astrofisica e Scienza dello Spazio, Via Piero Gobetti 93/3, Bologna 40129, Italy

\*Corresponding author. E-mail: giovanni.pratesi@unifi.it

(Received 19 July 2020; revision accepted 07 May 2021)

**Abstract**—The Cavezzo meteorite, which fell on January 1, 2020, is the first meteorite detected and recovered by the Italian PRISMA Fireball Network. Two specimens, weighing 3.12 g (specimen 1) and 52.19 g (specimen 2), were collected 3 days after the bolide was observed, thanks to an effective media campaign that encouraged the involvement of local people. The two specimens of this meteorite have not only completely different lithological characteristics but also a different geochemistry and oxygen isotopic composition as well. Specimen 1 is anomalous both for the textural–structural features, varying seamlessly from chondritic to “achondritic,” and a very unusual modal mineralogy—such as the relatively high amount of olivine (63.1 vol%), plagioclase (18.2 vol%), high-Ca pyroxene (10.3 vol%), and chlorapatite (2.1 vol%); and the unusually low content of low-Ca pyroxene (5.8 vol%), metal (0.1 vol%), and troilite (much lesser than 0.1 vol%)—although the compositional values for olivine (Fa 24.24 mol%) and low-Ca pyroxene (Fs 20.41 mol%) appear to be similar to those of the L chondrite group. Conversely, in specimen 2, not only the texture and the crystal chemistry but also the modal mineralogy (low-Ca pyroxene much more abundant than high-Ca pyroxene and occurrence of metal and sulfides) look like those of an ordinary L chondrite. The differences between the two specimens are also confirmed by geochemistry. The oxygen isotope composition of specimen 1 plots at the boundary between the H and L groups ( $\delta^{17}\text{O}_{\text{‰}}$  3.250;  $\delta^{18}\text{O}_{\text{‰}}$  4.736;  $\Delta^{17}\text{O}_{\text{‰}}$  0.788) whereas specimen 2 plots at the boundary of the L and LL fields ( $\delta^{17}\text{O}_{\text{‰}}$  3.737;  $\delta^{18}\text{O}_{\text{‰}}$  4.957;  $\Delta^{17}\text{O}_{\text{‰}}$  1.159). The bulk chemistry shows a different content of many minor and trace elements (including rare earth elements), such as a strong depletion of siderophile and chalcophile elements in specimen 1. The two specimens then do not contain fragments of each other, thus preventing us from classifying this “double face” meteorite as an ordinary chondrite breccia. In detail, specimen 1 can be considered a “xenolith” in which chondritic structure and igneous texture coexist without discontinuity, and therefore, it represents a previously unsampled portion of the L parent body. In summary, these findings support the classification of Cavezzo as an L5 anomalous chondrite.

## INTRODUCTION

In the field of meteorite studies, the recovery of a fresh fall is an important event, as it provides a rare opportunity to study pristine material almost devoid of any trace of terrestrial weathering. However, while any meteorite recovered on the ground after a visual observation of a fall provides an extraordinary amount of information due to its “unweathered” nature (W0, i.e., weathering grade = 0), there is a set of data—such as pre-atmospheric mass, velocity at infinity, entry angle, atmospheric trajectory—that a visual observation cannot provide. However, if the bolide is detected and monitored by an instrumental network capable of recording its entry into the atmosphere, not only can all these pre-atmospheric entry data be obtained, but the region of origin of the meteorite in the solar system can also be determined (Granvik and Brown 2018; Gardiol et al. 2021).

In Italy, such a network coordinated and managed by the National Institute of Astrophysics (INAF) has been operating since 2016. This network, named PRISMA (First Italian Network for Surveillance of Meteor and Atmosphere), consists of more than 50 all-sky cameras (among operative ones and in installation/purchasing phase), which perform a continuous monitoring of the Italian skies with the main scientific objective of detecting fireballs and bolides during nighttime hours (Barghini et al. 2019; Gardiol et al. 2019; Carbognani et al. 2020). Other networks exist around the world—starting with the historic imaging and subsequent recovery of the Příbram meteorite in 1959 (Ceplecha 1961)—all of them working with substantially the same goals as PRISMA, that is, the detection of fireballs and when possible the recovery of associated meteorites.

Nevertheless, the recovery of a meteorite still represents an exceptional event, although in the last few years, the refinement of detection and meteoroid trajectory calculation algorithms, and the increasing coverage of the cameras at global level has resulted in a significant increase in the number of meteorites being found. Notable recent examples are the Bunburra Rockhole “anomalous” eucrite that fell in 2007 (Bland et al. 2009; Benedix et al. 2017a), Mason Gully in 2010 (Dyl et al. 2016), Novato meteorite in 2012 (Jenniskens et al. 2014), Žďár nad Sázavou in 2014 (Kalašová et al. 2020; Spurný et al. 2020), Creston in 2015 (Jenniskens et al. 2019), Murrili in 2015 (Bland et al. 2016), Ejby in 2016 (Spurný et al. 2017b), Stubenberg in 2016 (Bischoff et al. 2017), Dishchii’bikoh in 2016 (Jenniskens et al. 2020), Hradec Kralove in 2016 (Spurný et al. 2017a), and Dingle Dell in 2016 (Benedix et al. 2017b).

On January 1, 2020, at 18:26:54 UT, a bolide was observed by many people living in northern and central Italy. This event was recorded by eight all-sky cameras of the Italian PRISMA Fireball Network. Analysis of the data revealed a track, inclined at about  $68^\circ$  with respect to the Earth’s surface, which started at an altitude of 75.9 km and ended at an altitude of 21.5 km (Gardiol et al. 2021). The pre-atmospheric velocity was relatively low ( $12.8 \text{ km s}^{-1}$ ), but the high fall angle gave rise to an intense ablation process that caused the bolide to shine with a maximum absolute magnitude of  $-9.5$ . The initial mass of the meteoroid has been estimated to be 3.5 kg and approximately 13 cm in size. During the fall, it went through a number of fragmentation episodes, particularly at 32.6 and 30.7 km height; then, at an altitude of 21.5 km, the meteoroid after deceleration to terminal velocity started the so-called dark flight. Further details about the dynamic fall parameters can be found in Gardiol et al. (2021).

Initial calculations suggested that some fragments of the original meteoroid had probably fallen to the ground in the area located between Rovereto sul Secchia, Disvetro, and Cavezzo (Modena province), in the middle of the Po valley. Three days after the event, on January 4, 2020, around 15:00 hours local time, Mr. Davide Gaddi was walking with his dog over the embankment of the Secchia river floodwater detention basin and was attracted by a small dark shiny stone. Since Mr. Gaddi had been informed through the media of the notice published by the PRISMA-INAF project about the possible fall of meteorites, after collecting the little specimen, he looked around and was able to find another specimen (the main mass) a few meters away (Lat.  $44^\circ 49' 43.80'' \text{N}$ , Long.  $10^\circ 58' 18.20'' \text{E}$ ).

The two specimens of this meteorite (Fig. 1)—named Cavezzo from the municipality where it fell—weigh 3.12 g (specimen 1) and 52.19 g (specimen 2). Both of them have been donated by the finder to the Italian National Institute of Astrophysics (INAF). The type specimen, represented by specimen 1 and a chip from specimen 2, has been given for deposit to the Natural History Museum of the University of Firenze. The main mass (specimen 2) has been given for deposit to the Museum of Planetary Sciences in Prato.

A detailed report on this fall was sent to the Nomenclature Committee of the Meteoritical Society. On September 5, 2020, the meteorite was approved as a new Italian meteorite with the name Cavezzo (Gattacceca et al. 2021).

In this article, we describe the mineralogy, petrography, and geochemistry of both specimens of Cavezzo meteorite, the first Italian meteorite detected and recovered thanks to the PRISMA Fireball

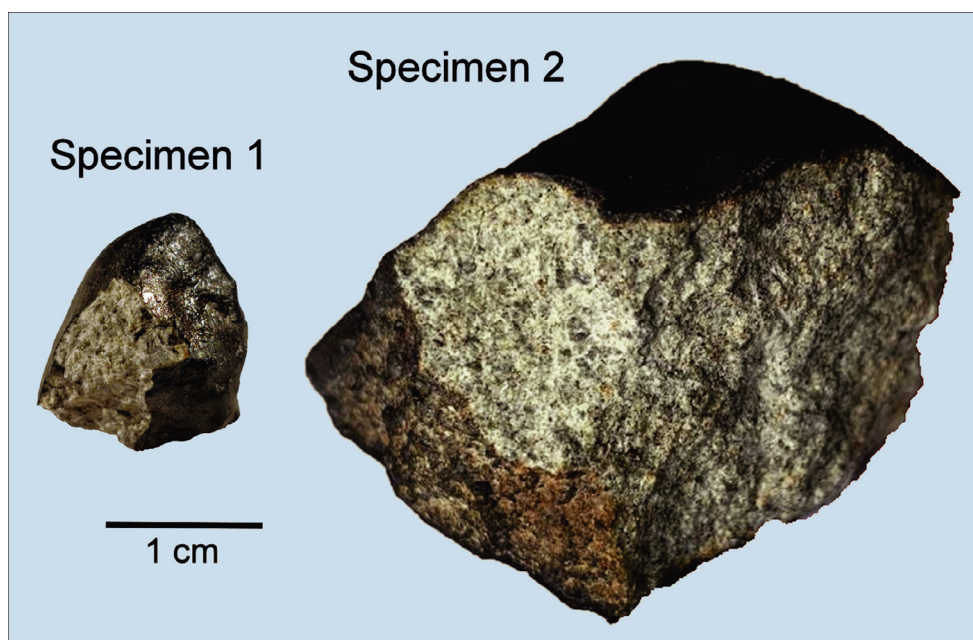


Fig. 1. A view of specimen 1 and specimen 2. Note the occurrence of a very thin shiny fusion crust in specimen 1 and a thicker matte black fusion crust in specimen 2. It is also interesting to note, in specimen 2, the presence of a surface (bottom left in the picture and Fig. S1 in supporting information) showing an incipient secondary fusion crust.

Network, a partner of the FRIPON Network (Colas et al. 2020).

## EXPERIMENTAL

### Samples

Immediately after the recovery, and before any handling, a structured light 3-D scanner (operating at the Laboratory of Vertebrate Palaeontology—Earth Sciences Department of the Università di Firenze) was used to capture data from the main mass of the meteorite. As can be seen in Fig. S2 in supporting information, this technique allows us to get a reliable 3-D image of specimen 2 that can be used to measure the size and volume of the object with great accuracy. Unfortunately, due to the small size of the specimen, this technique could not be used on specimen 1.

In the days following its recovery, the  $\gamma$ -ray activity was measured on specimen 2 (the only specimen of the two with a suitable mass) at the INAF Monte dei Cappuccini Laboratory in Torino (Taricco et al. 2006; Colombetti et al. 2013). This measurement has shown the presence of many cosmogenic radioisotopes, also confirming the presence of  $^{48}\text{V}$  (half-life of 15.97 days) that is an indisputable proof of the genuineness of the fall (Gardiol et al. 2021). The complete results of the radiometric measures of specimen 2 will be the subject of a forthcoming publication.

To carry out optical, scanning electron microscope (SEM), and electron probe microanalysis (EPMA) analyses, specimen 1 was entirely embedded in polyester resin due to its fragile and not particularly compact appearance. Conversely, specimen 2 was more compact, so just a single fragment was embedded in polyester resin. One mount (sample 1a) and two thin sections (samples 1b and 1c) were then obtained by cutting specimen 1. Likewise, one mount (sample 2a) and one thin section (sample 2b) were obtained by cutting the embedded fragment of specimen 2.

Samples 1a, 1c, and 2a are currently held by the Museo di Storia Naturale of the Università di Firenze (Inv. Nos. I3557-3, I3557-2, and I3613-2). The main mass (specimen 2) and samples 2b and 1b are deposited at the Museo di Scienze Planetarie in Prato (Inv. Nos. 8527, 8528, 8529). The latter samples have also been cataloged within the National Catalogue of Cultural Heritage (Cat. Nos. 0901332814, 0901332814-1, 0901332814-2) according to the Italian cataloging standard for Planetological Heritage—BNPL (Franza and Pratesi 2021a, 2021b). Both museums where the specimens are kept are included in the Meteoritical Society official repositories list.

### Techniques and Methods

Optical microscopy was performed at the Museo di Scienze Planetarie in Prato by means of a Zeiss Axioplan II optical microscope equipped with a Zeiss Axiocam camera.

SEM/EDS microanalyses and elemental mapping were undertaken at the MEMA laboratories of the Università di Firenze using a Zeiss EVO MA15 equipped with a 10 mm<sup>2</sup> Silicon Drift Detector (SDD) and OXFORD INCA 250 microanalysis software. An accelerating voltage of 15 keV and beam current of 10 nA were used to collect backscattered electron (BSE) images and energy-dispersive spectroscopy (EDS) maps, other than point analyses. Considering the different mean atomic number of all the phases, the BSE images were obtained in two different modes by changing the image settings, in particular brightness and contrast. This facilitated the discrimination of silicates on the one hand, and metal-oxide-sulfides on the other. Semiquantitative chemical data were then obtained from point analyses by converting count rates to concentrations using energy and beam calibration on a pure Co standard and factory quantitative standardizations for the elements of interest. Oxygen concentrations were calculated by stoichiometry for all phases except metals.

Modal mineralogy has been obtained by means of the instruments described above. This work was performed using the Oxford Inca Software Package, following procedures similar to those outlined by Gastineau-Lyons et al. (2002). Image analysis of 20 X-ray maps (1700 × 1200 μm wide) for each sample (sample 1a, sample 1c, and sample 2a) was undertaken. The procedure for image analysis involved searching on the map for the exact combination of elements present in the various phases. For each combination, the area occupied was estimated and the quantitative modal data then obtained using INCA 250 software. In the situation where two phases have the same elements (i.e., olivine and low-Ca pyroxene), the different Si/(Mg+Fe) ratios can be used to discriminate between them. The results are presented both in volume and in weight percentage to allow for comparison with previously calculated normative and measured modal abundances for ordinary chondrites (McSween et al. 1991; Gastineau-Lyons et al. 2002; Dunn et al. 2010a).

High resolution X-ray 3-D microtomography was performed at CRIST laboratories of the Università di Firenze, using a SKYSCAN 1172, in order to verify the distribution of Fe, Ni metals, and sulfides in the Cavezzo meteorite.

Quantitative analysis of the mineral phases present in Cavezzo was performed at the geochemistry laboratories of the Open University using a CAMECA SX-100 Electron Microprobe equipped with four wavelength-dispersive spectrometers at the laboratories of the Earth Sciences Department of the Università di Firenze using a JEOL JXA-8230 Electron Microprobe equipped with five spectrometers. In both cases,

operating conditions were 15 keV accelerating voltage, 20 nA beam current, a beam size of 5 and 1 μm (depending on the content of volatile elements in the phase to be analyzed), and data acquisition in wavelength-dispersive spectrometry (WDS) mode. The following standards have been used for the analyses: Si, Al, K on fspr-In5; Mg on for-BM4; Na on jad-BM4; Mn, Ca on bustamite; Cr on chromite; Ni on pentlandite; Cl on Tugtupite; P on apa-BM4; Ti on rut-BM4; S on pyri-PP5; Fe on AlmGnt; V on metallic V; Zn on metallic Zn.

As for minor and trace element analyses, one sample of specimen 1 and one sample of specimen 2 (each one of ~40 mg) were digested at the Open University using a standard HF-HNO<sub>3</sub> hotplate dissolution technique for trace element analysis, with an additional aqua regia stage to ensure complete sample digestion. In addition to the samples, six terrestrial reference materials (BIR-1, W2, DNC-1, AGV-1, RGM-1, BE-N) were digested for instrument calibration, along with the USGS BHVO-2 standard, which was used to monitor precision and accuracy of our measurements. All reagents used were Teflon distilled grade acids and Milli-Q H<sub>2</sub>O (>18.2 MΩ resistivity). After digestion, samples were diluted 1000-fold of the original powder weight in a 2% HNO<sub>3</sub> solution, prior to analysis. Trace element analysis was undertaken at the Open University, using an Agilent 8800 ICP-QQQ-MS triple quadrupole instrument. Most elements were analyzed in no gas or in He mode where interferences (e.g., oxides, doubly charged species) are a problem, with the rare earth elements (REE) measured in O<sub>2</sub> mode using a mass shift method. An online internal standard consisting of Be, Rh, In, Tm, and Bi was added to monitor and correct for instrument drift, and a monitor block consisting of the BHVO-2 standard and a 2% HNO<sub>3</sub> blank were also run before and after the samples. For the majority of elements, precision (assessed as the relative standard deviation [RSD] of the BHVO-2 measurements) was <2%, and accuracy was better than 5% (with the exception of Tl, Pb [10%], Li [15%], and Sn [65%]).

Oxygen isotopic analysis was undertaken at the Open University using an infrared laser-assisted fluorination system (Miller et al. 1999; Greenwood et al. 2017). Laser fluorination analyses were undertaken on two powdered samples produced by crushing and homogenizing two clean interior chips of the Cavezzo meteorite (one from specimen 1 and one from specimen 2) each weighing approximately 100 mg. For each sample, ~2 mg aliquots of the homogenized powder were loaded into an Ni sample block, which was then placed into a two-part chamber and made vacuum-tight using a compression seal with a copper gasket and a quick-release KFX clamp

(Miller et al. 1999; Greenwood et al. 2017). A 3 mm thick BaF<sub>2</sub> window at the top of the chamber allowed simultaneous viewing and laser heating of the samples. After sample loading, the cell was heated overnight to a temperature in excess of 70 °C to remove any adsorbed atmospheric moisture. Prior to fluorination, the system blank was systematically reduced by flushing the chamber with aliquots of BrF<sub>5</sub>, such that the final blank was <60 nanomols O<sub>2</sub>. Sample heating in the presence of BrF<sub>5</sub> was carried out using an integrated 50 W infrared CO<sub>2</sub> laser (10.6 μm) and video system mounted on an X–Y–Z gantry supplied by Photon Machines Inc. (Greenwood et al. 2017). After fluorination, the released O<sub>2</sub> was purified by passing it through two cryogenic (liquid nitrogen) traps and over a bed of heated KBr. The isotopic composition of the purified oxygen was analyzed using a Thermo Fisher MAT 253 dual-inlet mass spectrometer (mass resolving power ~200). Our current system precision based on repeat analyses of our obsidian internal standard is ±0.052‰ for δ<sup>17</sup>O, ±0.094‰ for δ<sup>18</sup>O, and ±0.017‰ for Δ<sup>17</sup>O (2σ; Starkey et al. 2016). Δ<sup>17</sup>O has been calculated as Δ<sup>17</sup>O = δ<sup>17</sup>O – 0.52 δ<sup>18</sup>O in order to directly compare our analyses of the two specimens of Cavezzo with the ordinary chondrite analyses of Clayton et al. (1991).

## RESULTS

The naturally exposed surface of specimen 1 has a white greenish color, a brittle structure, and does not show any visible trace of metal or sulfides. Attempts to ascertain whether specimens 1 and 2 were part of a single piece were inconclusive. Specimen 1 is neither particularly rounded nor oriented and shows a thin shiny black primary fusion crust as well as two broken surfaces (Fig. 1). Following the cut, we have been able to ascertain that the three samples (1a, 1b, 1c) obtained from specimen 1 show the same mineralogy, although there are differences in the apparent amount of chondrules between the various samples whose texture varies seamlessly from chondritic (Figs. 2 and S7 in supporting information) to “achondritic” (Figs. 2, S7, and 3). Moreover, specimen 1 shows no evidence of brecciation or discontinuity.

Specimen 2, which has a gray-whitish coloration, is very different from specimen 1 because it has a compact appearance and clearly contains metal and sulfides. Neither orientation nor rounding is visible (Fig. S2). Furthermore, its fusion crust looks thicker and has a more matte appearance than that of specimen 1. Specimen 2 appears to be homogeneous and shows no evidence of brecciation or fragmentation.

Both specimens show a lack of fusion crust on at least one of their sides due to fragmentation. Specimen 2 also displays a brown coloration on one side,

consistent with the fragmentation that occurred at a height of 30.7 km followed by exposure to heating during the last flight down to 21.5 km (Gardiol et al. 2021).

The distinctly different textures shown by specimens 1 and 2 are clearly illustrated in the photomosaics shown in Fig. 2.

## Petrography

### *Specimen 1*

The amount and appearance of chondrules vary significantly in the three samples of this specimen. In samples 1a and 1b (Figs. 2 and 4), the chondrules are well delineated and the boundary between chondrules and the enclosing matrix is easily distinguishable; nevertheless, in other portions of the specimen (sample 1c), chondrules seem to be scarce or even absent and an “achondritic” texture prevails (Fig. 3). This is the reason why a chondrule to matrix ratio is very difficult to provide. Some of the large chondrules within the sections are relatively intact (i.e., they exhibit ≥270° of arc and their texture is clearly visible) and have a diameter ranging from 800 to 2300 μm (mean 1400 μm); however, chondrule fragments (≤270° of arc) are more often present.

In textural variation, most of the chondrules appear to be barred olivine (BO) and display elongated subparallel bars of olivine separated by a crystallized mesostasis consisting of high-Ca pyroxene, plagioclase, and minor low-Ca pyroxene. Sometimes these BO chondrules consist of large (200–600 μm) olivine crystals, often fractured and with a continuous rim of olivine. These crystals are sometimes molded as large anhedral masses separated by a crystallized mesostasis containing the same minerals. In some porphyritic olivine (PO) chondrules where the olivine fills the entire chondrule, or in the large crystals outside the chondrules, a variety of poikilitic texture is present; in these cases, chadacrysts of plagioclase and pyroxenes are enclosed by oikocrysts of olivine that occupy all the available space. Both BO and PO chondrule types show diffuse tiny chromite veins and grains cross-cutting crystals of fractured olivine. Also, very few examples of granular olivine (GO) chondrules have been observed.

The interchondrule matrix consists mostly of large olivine crystals, up to 1–2 mm in diameter, with irregular rounded shapes separated by medium- to fine-grained aggregates of high-Ca pyroxene, olivine, and plagioclase, with minor low-Ca pyroxene. Plagioclase may also be found as rare, large (200–400 μm) crystals in the matrix. Chlorapatite crystals, ranging from 300 to 1000 μm, are visible everywhere. Metal is rare and can be found as small, rounded grains inside chromite veins

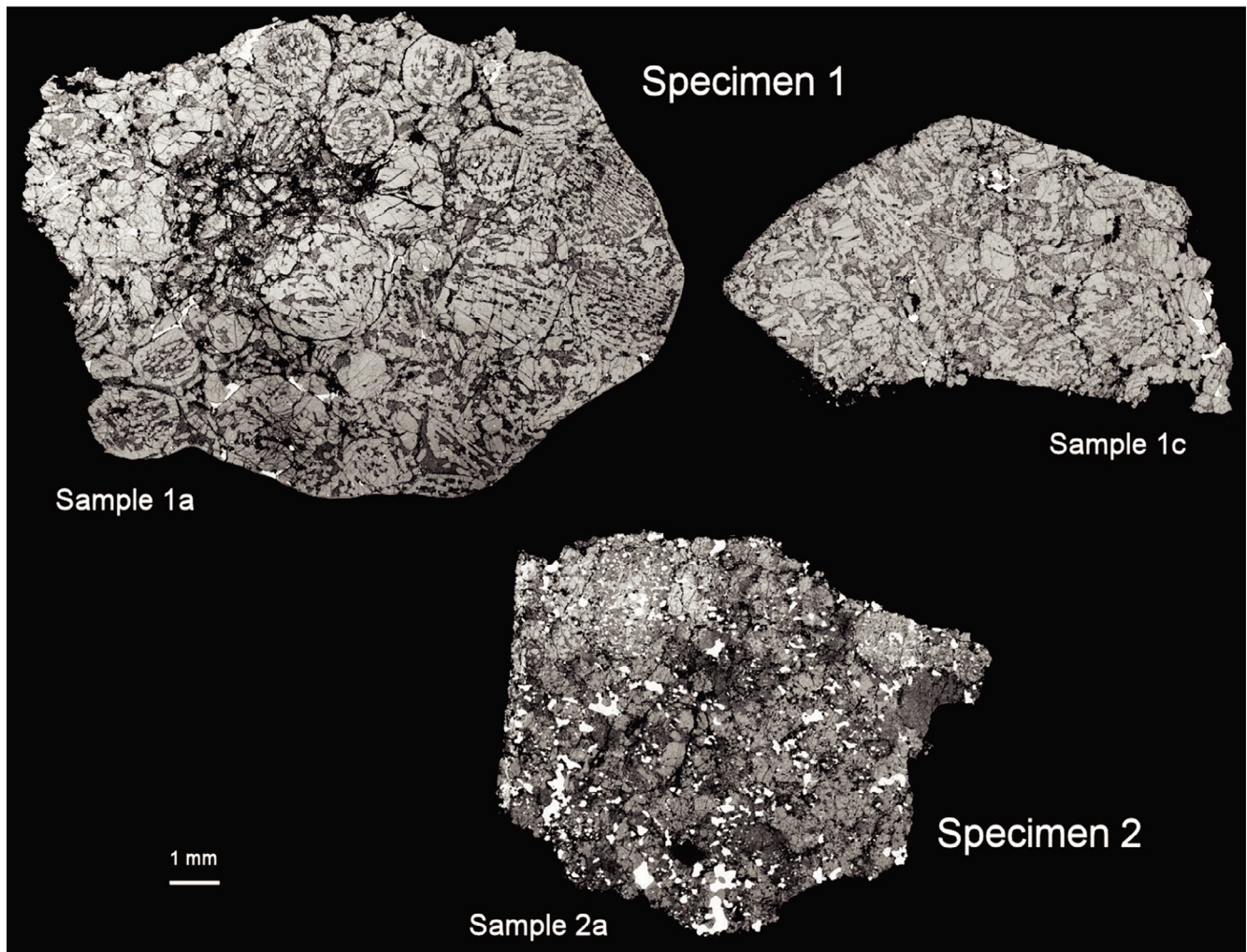


Fig. 2. BSE photomosaic of three samples of Cavezzo meteorite. In specimen 1, a transition from chondritic (sample 1a) to “achondritic” texture (sample 1c) is clearly visible. Conversely, specimen 2 presents a homogeneous texture that is characterized by the typical mineralogy of ordinary chondrites as shown in sample 2a.

(1–4  $\mu\text{m}$  in size), or as rare larger (20–100  $\mu\text{m}$ ) blebs or grains. Chromite is diffuse, mainly as small rounded grains (20–40  $\mu\text{m}$ ), and veins (1–2  $\mu\text{m}$  wide and up to 300  $\mu\text{m}$  long) or, more rarely, as larger blebs up to 100  $\mu\text{m}$ . Ilmenite is present as rare scattered blebs 20–40  $\mu\text{m}$  in size. Troilite is very rare since only one very tiny grain has so far been located.

#### *Specimen 2*

This specimen displays a texture mainly consisting of relic chondrules set in a fine- to medium-grained silicate matrix (Fig. 3). Few relic chondrules can be distinguished since the boundary between chondrules and matrix is in most cases not clearly delineated.

Chondrule types are mainly PO, porphyritic pyroxene (PP), and BO and range in diameter from 400 to 1600  $\mu\text{m}$ . They are distributed in a silicate matrix,

which accounts for about 85 vol% of the section, and the matrix is composed of chondrule and mineral fragments that constitute a fine- to medium-grained assemblage. PO chondrules have an approximately 2:1 olivine/pyroxene modal ratio and consist of olivine crystals 50–200  $\mu\text{m}$  in width. These crystals are separated by a fine-grained crystallized mesostasis mostly containing low-Ca pyroxene, with minor plagioclase and high-Ca pyroxene.

Some chondrules, ranging in diameter from 400 to 600  $\mu\text{m}$ , belong to the PP type and display a fine- to medium-grained aggregate of low-Ca and high-Ca pyroxene crystals, with minor plagioclase. A few BO chondrule fragments are present and these have a maximum width of 300  $\mu\text{m}$ , with narrow olivine bars (50  $\mu\text{m}$  in width) set in a plagioclase recrystallized mesostasis.

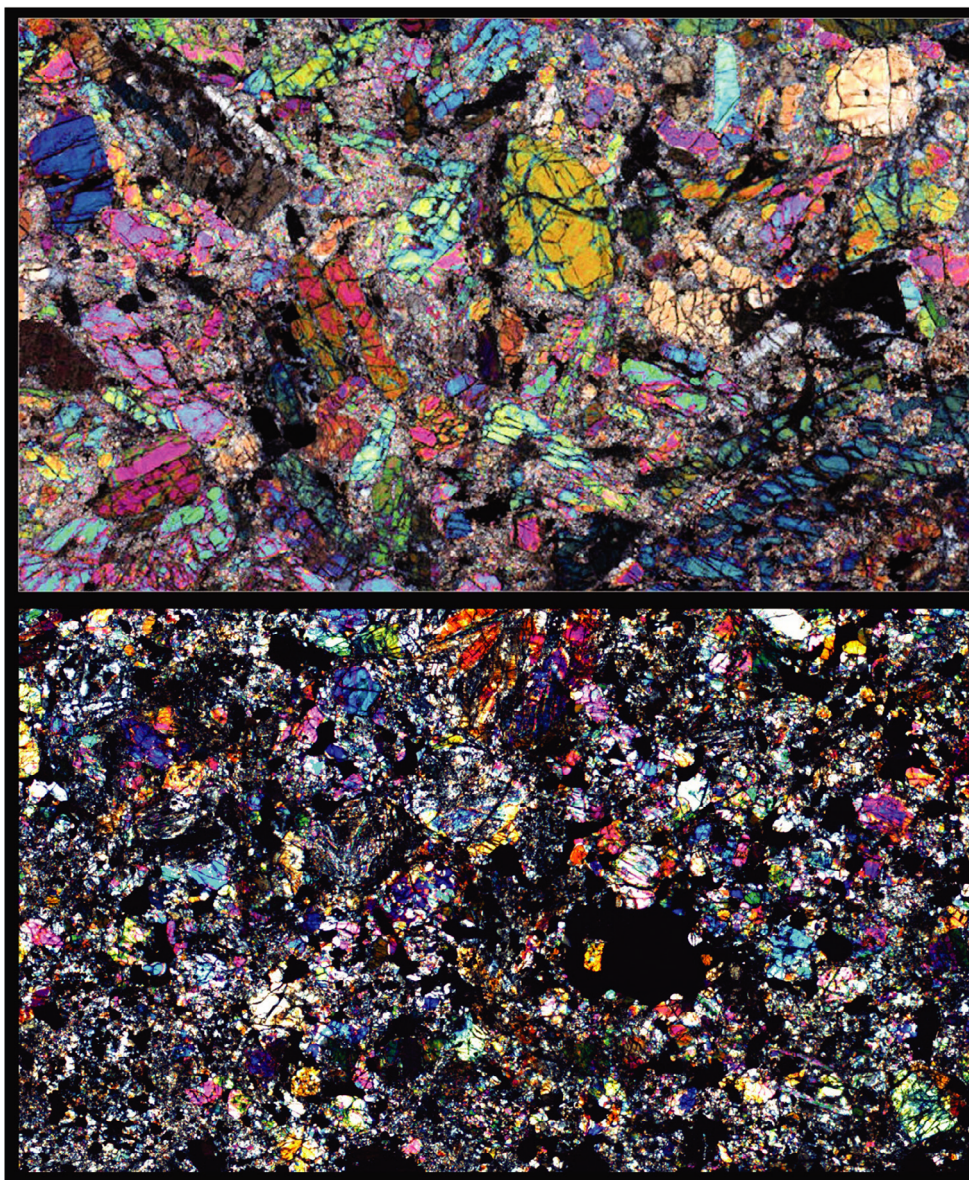


Fig. 3. Optical transmitted light (CP) photos of the two specimens of Cavezzo meteorite. Sample 1c (above) shows a texture characterized by large olivine crystals and the absence of chondrules whereas sample 2b (below) has a typical chondritic texture. Field width 6.3 mm.

The silicate matrix consists of medium-grained olivine and low-Ca pyroxene anhedral crystals, up to 600  $\mu\text{m}$  in length, with irregular shapes and intensively fractured, separated by a fine assemblage of olivine, low-Ca and high-Ca pyroxene, and plagioclase.

Metal is relatively abundant and can be found as large (100–500  $\mu\text{m}$ ) blebs or grains and small, rounded grains cross-cutting olivine crystals (1–4  $\mu\text{m}$  in size). Troilite mainly consists of dispersed, large blebs from 50 up to 300  $\mu\text{m}$  diameter. Phosphate and spinel grains, ranging from 100 to 200  $\mu\text{m}$  in size, are randomly dispersed throughout the section.

## Mineralogy and Mineral Chemistry

### *Specimen 1*

The modal mineralogy of samples 1a and 1c is, respectively, olivine (63.1 vol%; 67.0 wt%); plagioclase (18.2 vol%; 14.5 wt%); high-Ca pyroxene (10.3 vol%; 10.0 wt%); low-Ca pyroxene (5.8 vol%; 5.8 wt%); chlorapatite (2.1 vol%; 2.0 wt%); chromite (0.4 vol%; 0.5 wt%); ilmenite (0.1 vol%; 0.1 wt%); Fe, Ni (0.1 vol%; 0.1 wt%); and troilite (much less than 0.1 wt%).

Olivine is present both inside and outside chondrules and accounts for about 63.1 vol% (67.0 wt%) of the

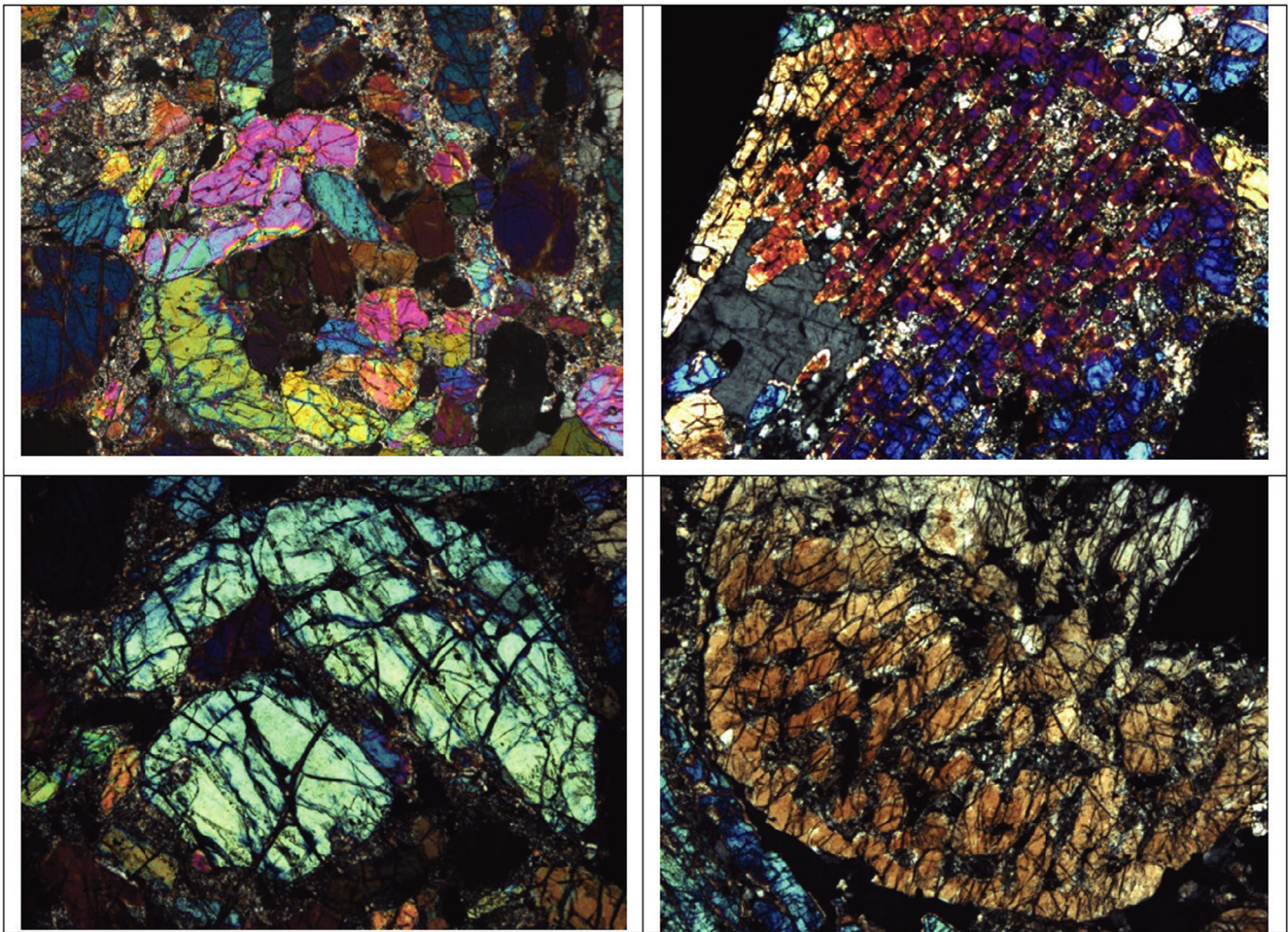


Fig. 4. Optical transmitted light photos (CP) of sample 1b: different types of chondrules as observed. In particular, the characteristics of porphyritic olivine (PO) and barred olivine (BO) chondrules can be easily seen. On the left (above and below): PO chondrules completely filled by large olivine crystals. On the right: BO chondrule with usual elongated and parallel olivine crystals (above); BO chondrule with segmented olivine crystals not more parallel.

specimen. Inside the chondrules, olivine may occur as fine-grained (10–100  $\mu\text{m}$ ) euhedral and subhedral grains, along with high-Ca pyroxene and plagioclase, in the interstitial areas among the larger coarse-grained (500–1500  $\mu\text{m}$ ) olivine aggregates that join together to take up most of the space inside the chondrules. Outside the chondrules, the olivine occurs as rounded grains, fragments, or large subhedral crystals ranging up to 2000  $\mu\text{m}$  (Fig. 5). Although the crystals are often heavily fractured, they are not mosaicized and do not show undulose extinction.

The composition of all the olivine analyzed (both inside and outside the chondrules) is essentially homogeneous, with a very limited compositional range and no appearance of rim to core variation (mean of 28 analyses,  $\sigma\text{-Fa mol}\% = 0.19$ ). EPMA analyses, as reported in Table 1, provide a mean  $\text{Fa}_{24-6}$  content in olivine. Many minor elements fall below the detection

limit ( $\text{TiO}_2$ ,  $\text{Al}_2\text{O}_3$ ,  $\text{Cr}_2\text{O}_3$ ,  $\text{CaO}$ ) with the exception of a moderate MnO content (0.47 wt%). NiO, CoO, and  $\text{V}_2\text{O}_5$  have also been analyzed, but their amounts are always below detection limit ( $\leq 0.02$  wt%).

Pyroxene, although less abundant than olivine, is found throughout the studied sections in specimen 1 and their total quantity is 16.1 vol%. It is noteworthy that in specimen 1, unlike other ordinary chondrites, low-Ca pyroxene is less abundant than high-Ca pyroxene, accounting for 5.8 vol% (5.8 wt%) and 10.3 vol% (10.0 wt%), respectively.

Inside the chondrules, in the interstitial areas between the larger olivine crystals (coarse-grained), pyroxenes coexist in a granular texture along with olivine (fine-grained) and plagioclase. In these areas (Fig. 6), high-Ca pyroxene forms clearly visible and well-outlined grains (up to 200  $\mu\text{m}$ ), while low-Ca pyroxene tends to appear as small anhedral grains



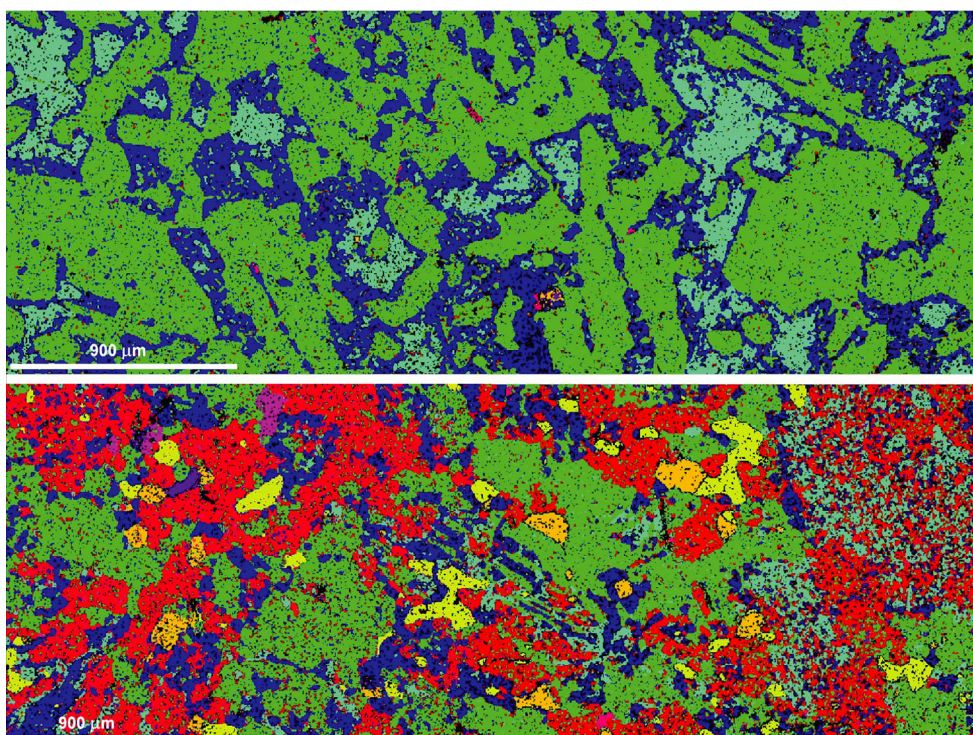


Fig. 5. Phase maps representative of specimen 1 (above) and specimen 2 (below). In particular, the upper image shows the “achondritic” texture of the sample 1c whereas the lower image refers to the sample 2b which presents, everywhere, the usual mineralogy and petrography of the L ordinary chondrites. In the sample 1, the olivine (green) is much more abundant. Other phases visible in both the images are low-Ca pyroxene (red), plagioclase (blue), high-Ca pyroxene (cyan), and Ca-phosphates (fuchsia). Iron (orange) and troilite (yellow) are much more abundant in specimen 2 (below).

(usually around 50  $\mu\text{m}$ ) without defined borders within the high-Ca grains. Outside the chondrules (Fig. 6), there is only one portion of specimen 1a where relatively large crystals (up to 100  $\mu\text{m}$ ) of low-Ca pyroxenes occur, although they continue to exist intermixed with high-Ca pyroxenes and not as separated, outlined grains.

Pyroxenes, as shown in Table 1, regardless of their appearance, size, or location, are characterized by a very homogeneous composition and define two very narrow compositional fields ( $\sigma\text{-Fs mol}\% = 0.26$ ). Low-Ca pyroxene is an enstatite, very poor in Wo component ( $\text{En}_{78.2}\text{Fs}_{20.4}\text{Wo}_{1.4}$ ), that may contain other minor elements:  $\text{TiO}_2$  0.24 wt%,  $\text{Al}_2\text{O}_3$  0.15 wt%,  $\text{Cr}_2\text{O}_3$  0.13 wt%,  $\text{MnO}$  0.49 wt%. The more abundant high-Ca pyroxene is a diopside-augite ( $\text{En}_{48.0}\text{Fs}_{7.8}\text{Wo}_{44.2}$ ) (Table 1) that, aside from some rare Fe-enriched rims, shows a lower FeO content compared to low-Ca pyroxene. Again, there are detectable minor elements:  $\text{TiO}_2$  0.58 wt%,  $\text{Al}_2\text{O}_3$  0.57 wt%,  $\text{Cr}_2\text{O}_3$  0.88 wt%,  $\text{MnO}$  0.21 wt%,  $\text{Na}_2\text{O}$  0.59 wt%.

In specimen 1, recrystallized feldspathic mesostasis accounts for 18.2 vol% and 14.5 wt%. It may occur as

allotriomorphic patches among olivine crystals or as anhedral grains in the fine-grained assemblage of olivine and high- and low-Ca pyroxenes. It is noteworthy that there are no differences, either textural or mineralogical, between plagioclase found outside or inside the chondrules.

Quantitative compositional data show that plagioclase has a relatively homogeneous composition (Table 1) that is usually Na-rich, with an anorthite content ranging between 9.8 and 12.1 mol% and an FeO content of 0.40 wt% average content ( $\text{An}_{11}\text{Ab}_{83}\text{Or}_6$ ). Other elements (Ti, Mn, Cr, Ni, V) were below the detection limit.

A very interesting feature of specimen 1 is the presence of relatively abundant apatite (2.1 vol%; 2.0 wt%), namely chlorapatite. It appears to be not homogeneously distributed throughout the mapped areas as it looks to be much more abundant in the area where chondrules are not visible (Fig. 2). To confirm this, it is only found outside the chondrules (Fig. 6b), in the interstitial area between crystals of olivine, as unusually large grains ranging from 300  $\mu\text{m}$  up to 800  $\mu\text{m}$  (mean size 500  $\mu\text{m}$ ). These grains are generally

Table 1. Average compositions of the major phases in the Cavezzo meteorite. Data in wt%.

	Olivine				Low-ca pyroxene				High-ca pyroxene				Feldspar			
	Specimen 1		Specimen 2		Specimen 1		Specimen 2		Specimen 1		Specimen 2		Specimen 1		Specimen 2	
	Mean	SD	Mean	SD	Mean	SD	Mean	SD	Mean	SD	Mean	SD	Mean	SD	Mean	SD
n	28		22		18		22		25		20		22		24	
SiO <sub>2</sub>	38.65	0.81	38.27	0.85	55.78	0.80	55.55	0.78	53.82	1.05	53.97	1.03	64.75	1.22	64.54	1.20
TiO <sub>2</sub>	0.02		<0.02		0.24	0.05	0.17	0.05	0.58	0.08	0.45	0.08	0.05		0.05	
Al <sub>2</sub> O <sub>3</sub>	<0.03		<0.03		0.15	0.03	0.16	0.03	0.57	0.03	0.48	0.02	21.12	0.36	20.72	0.38
Cr <sub>2</sub> O <sub>3</sub>	0.02		<0.02		0.13	0.04	0.11	0.04	0.88	0.05	0.78	0.05	0.03		<0.02	
FeO	22.62	0.46	22.73	0.48	12.98	0.41	13.73	0.40	4.73	0.17	4.84	0.16	0.40	0.10	0.37	0.11
MnO	0.47	0.04	0.47	0.04	0.49	0.04	0.48	0.04	0.21	0.04	0.21	0.04	<0.02		<0.02	
MgO	38.61	0.64	38.99	0.62	28.96	0.38	29.41	0.37	17.03	0.18	17.31	0.17	<0.03		<0.03	
CaO	0.03		0.02		0.72	0.09	0.74	0.10	21.85	0.28	21.48	0.26	2.35	0.06	2.11	0.05
Na <sub>2</sub> O	<0.03		<0.03		<0.03		<0.03		0.59	0.05	0.56	0.05	10.06	0.31	10.13	0.33
K <sub>2</sub> O	<0.02		<0.02		0.30	0.05	<0.02		<0.02		<0.02		0.99	0.23	0.96	0.25
Total	100.35		100.46		99.75		100.36		100.27		100.08		99.76		98.87	
Fa	24.61	0.32	24.52	0.31												
Range	24.00–25.23		24.32–24.87													
Fs					20.41	0.38	20.99	0.39	7.79	0.21	7.95	0.22				
Range					20.14–20.64		20.54–21.57		6.79–8.39		7.14–8.82					
En					78.19	0.41	77.61	0.40	47.98	0.20	48.66	0.20				
Range					77.77–78.66		77.20–77.89		47.51–48.41		48.35–48.96					
Wo					1.40	0.18	1.40	0.19	44.23	0.27	43.39	0.28				
Range					1.02–1.85		0.99–1.77		43.45–45.20		42.22–44.22					
An													10.82	0.38	9.76	0.39
Range													9.78–12.12		9.26–10.05	
Or													5.39	0.80	5.29	0.82
Range													4.31–7.30		3.74–6.75	

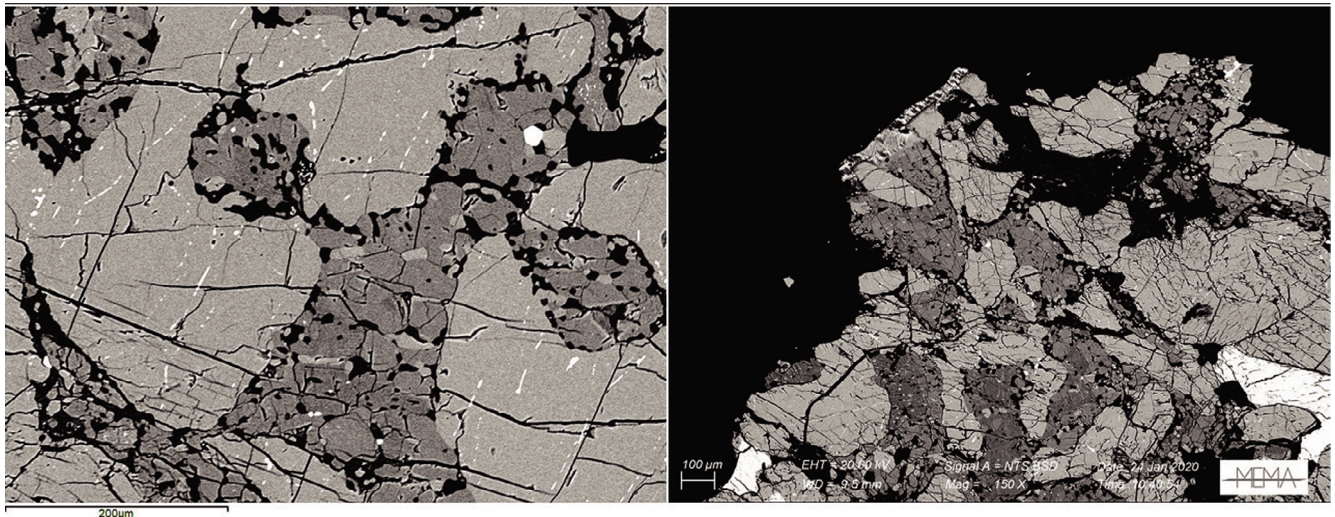


Fig. 6. BSE images of mineral phases in sample 1a. On the left (a): detail of a chondrule. The interstitial areas among the coarse-grained olivines are occupied by a granular assemblage of olivine (light gray), plagioclase (black), high-Ca pyroxene (gray), and low-Ca pyroxene (dark gray). On the right (b): an area of the sample outside the chondrules. Despite the somewhat larger size of the low-Ca pyroxenes, the relationship among the phases does not change significantly. The white grains at the bottom left and bottom right are chlorapatite.

located at or near the boundaries of olivine crystals, sometimes inside those feldspar patches that lack a granular assemblage of olivine, plagioclase, and low- and high-Ca pyroxene.

Members of the spinel group are dominated by the presence of chromite (0.4 vol%; 0.5 wt%) with sizes usually ranging from a few micrometers to hundreds of micrometers, occurring in olivine as small, rounded grains (Fig. 7a) or tiny veins (Fig. 7b), or inside plagioclase as subhedral to anhedral grains often sharing a border with olivine or metal (Figs. 7e, 7f, and 7g). Moreover, chromite may also be present in the form of micrometer- to submicrometer-size grains in the plagioclase (Figs. 7c and 7h). No zoning is visible in the grains and the uniform composition gives the mean values visible in Table 2.

As suggested by Rubin (1997), ilmenite occurs as a rare phase in ordinary chondrites; indeed, even in specimen 1, it accounts for only 0.1 vol% (0.1 wt%). Small, well-defined grains (20–50  $\mu\text{m}$ ) associated with kamacite or taenite (Figs. 7e and 7f) show the following mean composition:  $\text{TiO}_2$  53.85 wt%;  $\text{FeO}$  38.25 wt%;  $\text{MgO}$  3.19 wt%;  $\text{MnO}$  0.97 wt%;  $\text{V}_2\text{O}_5$  0.37 wt%;  $\text{Cr}_2\text{O}_3$  0.08 wt%. Although the ratio  $\text{Ti}/\text{Fe}$  is a bit different from the ideal formula, nevertheless, it is in the range of values provided by Snetsinger and Keil (1969).

Aside from a unique small grain of troilite, neither pentlandite nor pyrrhotite has been found in specimen 1.

Fe-Ni metals are very rare opaque phases in the meteorite, accounting for only 0.1 vol% (0.1 wt%). They are unaltered because the sample was found only 3 days after it had fallen. All these phases have been found through a detailed investigation of samples 1a, 1b, and 1c (Figs. 7b–g). Iron (kamacite), occurring as grains of variable size (from a few micrometers to 200–300  $\mu\text{m}$ ) in olivine and plagioclase, is usually associated with chromite (Figs. 7b and 7c), taenite (Fig. 7d), and tetrataenite as well (Fig. 7g). As shown in Table 2, iron contains Fe 94.56 wt%; Ni 4.26 wt%; and Co 1.59 wt%, whereas the Si-content is  $\leq 0.05$  wt% (below the detection limit of our analysis). Taenite usually occurs in the spaces occupied by plagioclase, as distinct grains (from tens of micrometers to 200–300  $\mu\text{m}$ ) along with iron (Fig. 7d); sometimes, grains of chromite can also be joined to grains of taenite (Fig. 7f). Analyses yield the following mean composition for taenite: Fe 84.26 wt%; Ni 14.97 wt%; Co 0.90 wt%. Detectable amounts of Cu are also present. Tetrataenite also occurs in specimen 1 as small, well-defined grains (10–60  $\mu\text{m}$ ) usually associated with iron (Figs. 7e and 7g).

### Specimen 2

A modal mineralogical analysis has been performed also on specimen 2. The percentage calculated for each phase in the analyzed areas of the sample specimen 2a has been averaged and the results are as follows: olivine (38.7 vol%; 38.1 wt%); plagioclase (15.0 vol%; 11.0 wt%); high-Ca pyroxene (5.5 vol%; 5.0 wt%); low-Ca pyroxene (29.7 vol%; 27.7 wt%); chlorapatite (0.2 vol%; 0.1 wt%); merrillite (0.3 vol%; 0.3 wt%); chromite (1.3 vol%; 1.6 wt%); Fe, Ni (4.5 vol%; 9.9 wt%); troilite (4.8 vol%; 6.3 wt%).

Although chondrules are not clearly delineated, olivine is present both inside and outside relic chondrules and accounts for about 38.7 vol% (38.1 wt%) of the specimen. Inside chondrules, olivine occurs as medium-grained (50–200  $\mu\text{m}$ ) euhedral grains, along with pyroxene and plagioclase. Outside chondrules, olivine may occur as fragments or large subhedral crystals ranging up to 600  $\mu\text{m}$ , often heavily fractured, although they do not show signs of shock-induced deformation such as mosaicism or undulose extinction.

The composition of all the olivine analyzed is essentially homogeneous, with a very limited compositional range and no appearance of rim to core variation (mean of 22 analyses,  $\sigma\text{-Fa}$  mol% = 0.15). EPMA analyses, as reported in Table 1, provide a mean  $\text{Fa}_{24.5}$  content in olivine. Many minor elements fall below detection limits ( $\text{TiO}_2$ ,  $\text{Al}_2\text{O}_3$ ,  $\text{Cr}_2\text{O}_3$ ,  $\text{CaO}$ ,  $\text{NiO}$ ,  $\text{CoO}$ ,  $\text{V}_2\text{O}_5$ ), with the exception of a moderate MnO content (0.47 wt%).

Pyroxenes are dispersed throughout the studied section of specimen 2 and their total amount accounts for about 35.2 vol%. The low-Ca pyroxene versus high-Ca pyroxene ratio is consistent with that of other ordinary chondrites, since low-Ca pyroxene is more abundant than high-Ca pyroxene, accounting for 29.7 vol% (27.7 wt%) and 5.5 vol% (5.0 wt%), respectively.

Inside PO chondrules, pyroxenes are present in a fine-grained texture along with plagioclase. In these areas, low-Ca pyroxene tends to occur as small anhedral grains without defined borders intermingled with tiny plagioclase grains. In PP chondrules, pyroxenes are present both as an intergrowth of low-Ca and high-Ca pyroxene anhedral grains or as medium-grained aggregates of the same phases. Outside the chondrules, pyroxenes appear both as a fine aggregate of low- and high-Ca pyroxene mixed with plagioclase grains or as medium to large (up to 200  $\mu\text{m}$ ) euhedral crystals of low-Ca pyroxene.

As displayed in Table 1, pyroxenes are characterized by a very homogeneous composition and define two very narrow compositional fields ( $\sigma\text{-Fs}$  mol% = 0.27). Low-Ca pyroxene is an enstatite, very

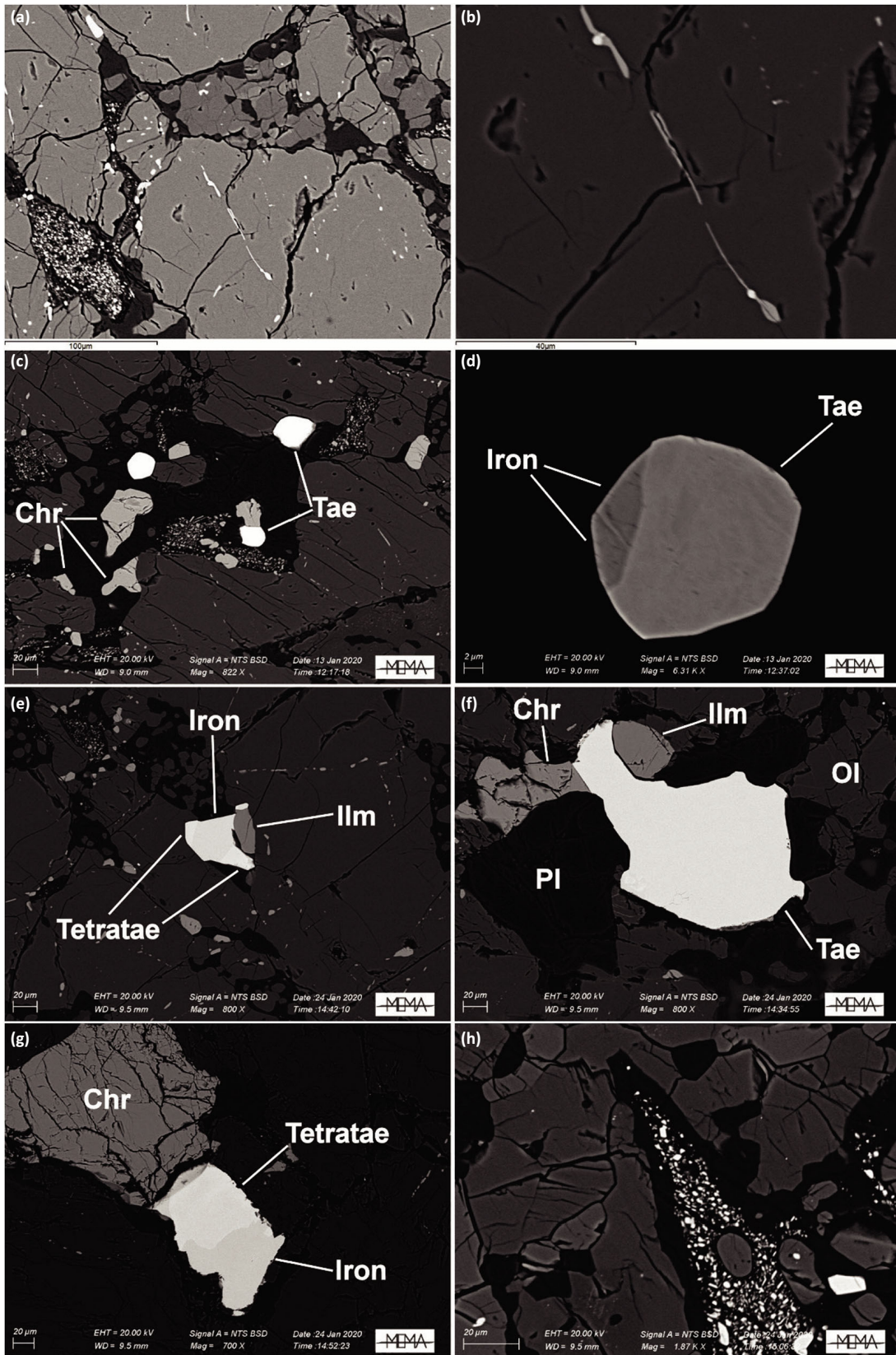


Fig. 7. BSE images of mineral phases in sample 1a. a) Veins and grains of chromite in olivine. b) A detailed view of the vein reveals that it is composed of chromite with the exception of two small grains (white) that are instead composed of iron (*kamacite*). c) Grains of iron (*kamacite*) and chromite in plagioclase (dark gray). d) A metallic grain composed of iron (*kamacite*) and taenite. e) Metallic grain in the center: tetrataenite, iron (*kamacite*), ilmenite, chromite. f) Taenite, chromite, ilmenite grains along with silicates. g) Chromite, iron (*kamacite*), and tetrataenite. h) Micrometer to submicrometer-sized chromite grains in plagioclase.

Table 2. Average compositions of the opaque phases in the Cavezzo meteorite. Data in wt%.

	Iron ( <i>kamacite</i> )				Taenite				Troilite				Spinel <sup>2</sup>			
	Specimen 1		Specimen 2		Specimen 1		Specimen 2		Specimen 1		Specimen 2		Specimen 1		Specimen 2	
	Mean	SD	Mean	SD	Mean	SD	Mean	SD	Mean	SD	Mean	SD	Mean	SD	Mean	SD
n	3 <sup>1</sup>		10		2 <sup>1</sup>		10		0		13		3 <sup>1</sup>		12	
Fe	94.56	–	93.66	1.02	84.26	–	86.09	0.78	–	–	63.60	0.30	31.95	–	31.88	0.34
Ni	4.26	–	6.12	0.38	14.97	–	13.04	0.27	–	–	<0.02	–	<0.02	–	<0.02	–
V	<0.02	–	<0.02	–	<0.02	–	<0.02	–	–	–	<0.02	–	0.87	–	0.70	0.04
Zn	0.03	–	0.02	–	<0.02	–	<0.02	–	–	–	<0.02	–	0.48	–	0.51	0.11
Co	1.59	–	1.18	0.20	0.90	0.15	0.83	0.18	–	–	0.11	0.02	<0.02	–	<0.02	–
Cu	<0.02	–	<0.02	–	0.09	0.01	0.08	0.02	–	–	<0.02	–	<0.02	–	<0.02	–
Si	<0.02	–	<0.02	–	<0.02	–	<0.02	–	–	–	<0.02	–	<0.02	–	<0.02	–
Mg	–	–	–	–	–	–	–	–	–	–	–	–	2.23	–	2.35	0.11
Al	–	–	–	–	–	–	–	–	–	–	–	–	5.41	–	5.55	0.13
Ca	–	–	–	–	–	–	–	–	–	–	–	–	<0.02	–	<0.02	–
Mn	<0.02	–	<0.02	–	<0.02	–	<0.02	–	–	–	<0.02	–	0.47	–	0.38	0.03
Cr	0.04	–	<0.02	–	<0.02	–	<0.02	–	–	–	<0.02	–	55.58	–	55.85	0.71
Ti	0.04	–	0.02	–	0.02	–	<0.02	–	–	–	<0.02	–	3.47	–	3.06	0.14
S	–	–	–	–	–	–	–	–	–	–	36.13	0.24	–	–	–	–
Total	100.51	–	101.02	–	100.27	–	100.05	–	–	–	99.84	–	100.50	–	100.29	–

<sup>1</sup>The standard deviation was not calculated when <4 grains were analyzed.

<sup>2</sup>Results in oxides wt%.

poor in Wo component (En<sub>77.6</sub>Fs<sub>21.0</sub>Wo<sub>1.4</sub>), that may contain other minor elements: TiO<sub>2</sub> 0.17 wt%, Al<sub>2</sub>O<sub>3</sub> 0.16 wt%, Cr<sub>2</sub>O<sub>3</sub> 0.11 wt%, MnO 0.48 wt%. High-Ca pyroxene is a diopside–augite (En<sub>48.7</sub>Fs<sub>7.9</sub>Wo<sub>43.4</sub>; Table 1). Minor detectable elements are TiO<sub>2</sub> 0.45 wt%, Al<sub>2</sub>O<sub>3</sub> 0.48 wt%, Cr<sub>2</sub>O<sub>3</sub> 0.78 wt%, MnO 0.21 wt%, and Na<sub>2</sub>O 0.56 wt%.

In specimen 2, plagioclase accounts for 15.0 vol% and 11.0 wt%. It occurs in two different assemblages: in PO chondrules relics as a recrystallized feldspathic mesostasis intermixed with low-Ca pyroxene and surrounding olivine crystals; in the matrix as anhedral grains, up to 200 μm, in the fine- to medium-grained assemblage of olivine, and low- and high-Ca pyroxenes.

Quantitative compositional data show that plagioclase has a homogeneous composition (Table 1) that is usually Na-rich, with an anorthite content ranging between 9.26 and 10.05 mol% (mean An<sub>9.8</sub>Ab<sub>84.9</sub>Or<sub>5.3</sub>) and an FeO content of 0.37 wt%.

Both merrillite and chlorapatite occur in specimen 2 and account, on the whole, for 0.5 vol% (0.4 wt%).

These phases can be found as dispersed grains in the matrix and range in size from 100 to 200 μm.

Chromite is a minor phase (accounting in specimen 2 for 1.3 vol%; 1.6 wt%) with sizes usually ranging from a few micrometers to few hundreds of micrometers, occurring as subhedral to anhedral grains in the matrix (Figs. 8f–h). No zoning is visible in the grains and the uniform composition gives the mean values visible in Table 2.

Troilite can be found as medium to large grains and blebs from 50 up to 300 μm in size, mostly in the matrix, and accounts for 4.8 vol% (6.3 wt%) of the section. As concerns the composition, it is a Ni-poor troilite with Ni and Cr below the detection limits, whereas Co is about 0.11 wt% (Table 2). Aside from troilite, no other sulfides, such as pentlandite or pyrrhotite, are present in specimen 2.

As shown by X-ray tomography (Fig. S8 in supporting information), in specimen 2 Fe, Ni metal phases are common and homogeneously distributed throughout the sample. Their total amount (4.5 vol%, 9.9

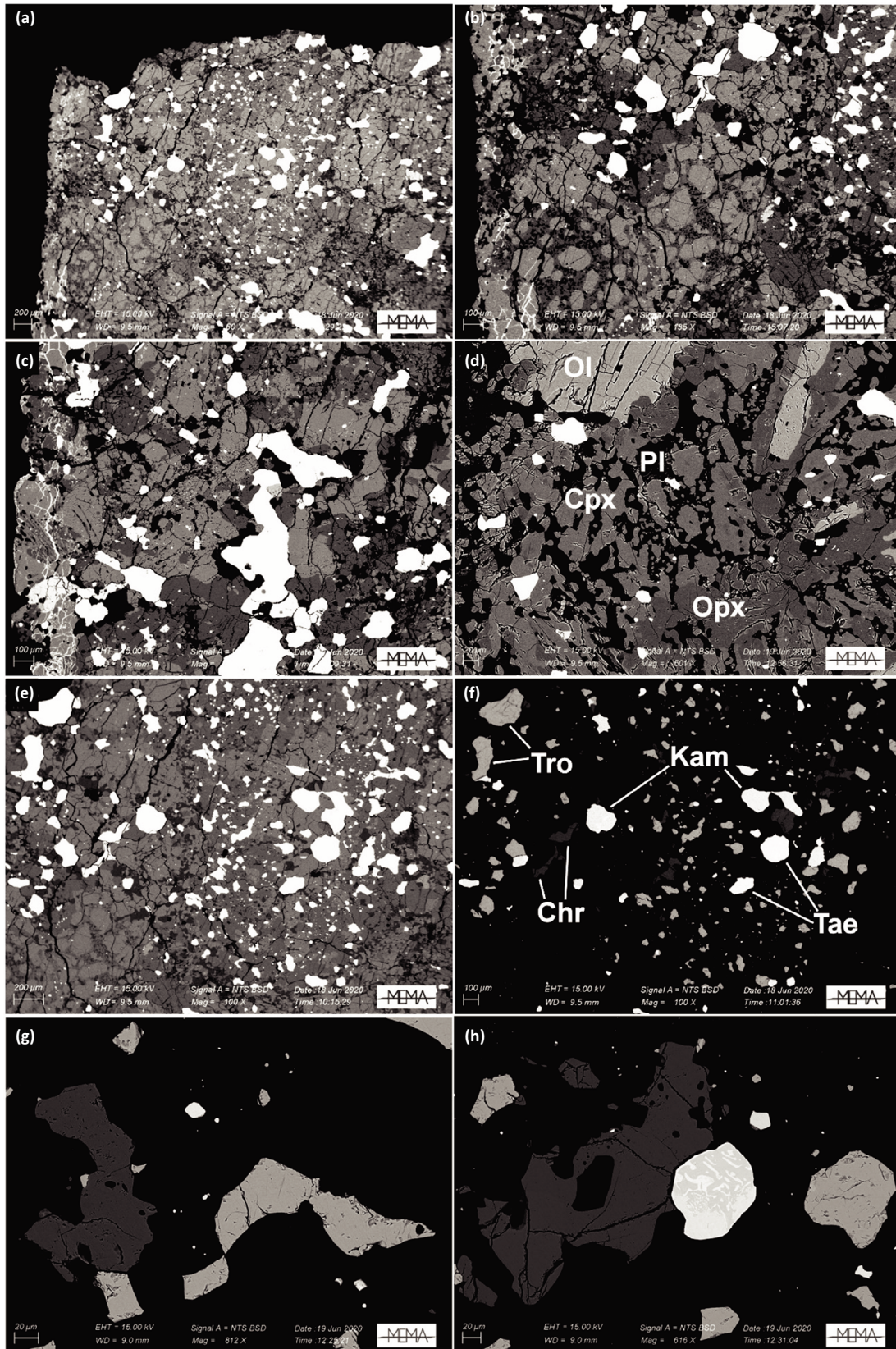


Fig. 8. BSE images of mineral phases in sample 2a. a) General appearance of the sample. b) In the enlargement of the previous image, two PO chondrules can be viewed. c) Assemblage of metal and silicates. d) Relationships among olivine, high-Ca pyroxene (Cpx), and low-Ca pyroxene (Opx). e, f) Opaque phase and their relationships with silicate minerals. g) Chromite grain (dark gray) along with troilite grains (gray). h) Chromite (dark gray); troilite (gray); and, in the center of the image, a plessitic grain of iron (kamacite), taenite, and tetrataenite.

wt%) significantly differs from specimen 1. These phases can be found mainly in the matrix as large blebs or tiny droplets cross-cutting olivine crystals. Iron (kamacite) occurs in the silicate matrix as grains of variable size (from few micrometers to 200–300  $\mu\text{m}$ ) usually associated with chromite, taenite, and tetrataenite (Figs. 8f and 8h).

Iron (kamacite) contains Fe 93.66 wt%, Ni 6.12 wt%, and Co 1.18 wt% (mean composition), whereas the Si-content is below the detection limit (Table 2). Taenite may occur associated with kamacitic iron or in single grains (Fig. 8f) ranging from tens of micrometers to 200–300  $\mu\text{m}$ . The following mean composition has been detected for taenite: Fe 86.09 wt%; Ni 13.04 wt%; Co 0.83 wt%. Detectable amounts of Cu are also present. Other elements are below detection limit (Table 2). Tetrataenite also occurs in specimen 2, either intimately associated in plessitic structure with iron (kamacite) and taenite (Fig. 8h) or as blebs and droplet (10–20  $\mu\text{m}$ ).

## Chemistry

### Minor and Trace Elements

Minor and trace elements have been analyzed both for specimen 1 and specimen 2. Of the 40 elements that were measured, only one (Ti) was below the detection limit. Concentration values, as well as the RSD, are reported in Table 3.

Considering the CI-normalized trace elements, we can observe strong differences occurring between the two specimens in the amounts of low-, medium-, and high-volatility elements (Fig. 9; Table 3). When compared to other ordinary chondrites, both Cavezzo specimens show some significant differences from the H, L, and LL groups, with specimen 1 showing strongly divergent compositional trends (Fig. 9). In particular, specimen 1 appears to be strongly depleted in Mo, Ni, Co, Cu, Sn, and moderately depleted in Sb, Ga, and Cs. It is noteworthy that Cr is slightly depleted in both specimens, although in specimen 1 it is at a lesser amount, whereas a clear depletion of Pb and Cs occurs in specimen 2. As concerns U, specimen 1 displays a relatively high content (compared to ordinary chondrites).

Surprisingly, the CI-normalized REE patterns (see Fig. 11) of specimen 1 and specimen 2 seem to be affected by a complementary correlation. In comparison with ordinary chondrites, the content of both LREE and HREE is higher in specimen 1. In contrast, their contents in specimen 2 are slightly lower than they are

in ordinary chondrites. Significantly, the Eu anomaly is negative in specimen 1 and positive in specimen 2.

### Oxygen Isotopic Composition

Both the specimens of Cavezzo meteorite were analyzed during two distinct analytical sessions and the results are given in Table 4 and plotted in Fig. 11. During both sessions, the two specimens gave essentially the same oxygen isotopic compositions (Fig. 11). Specimen 1 plots close to the junction of the H and L fields whereas specimen 2 plots on the opposite side, close to the boundary between the L and LL fields.

## DISCUSSION

### Petrography and Mineralogy

Petrographic and mineralogical features of specimen 1 differ in many ways from those of other ordinary chondrites. Starting with the chondrules, in specimen 1a, they have an abundance of about 70 vol% (but only 20 vol% in specimen 1c), which is in the range of ordinary chondrites (Brearley and Jones 1998; Grady et al. 2014) whereas their diameters (ranging from 800 to 2300  $\mu\text{m}$ ) appear larger than the range reported for H and L ordinary chondrites but similar to those suggested by Friedrich et al. (2015) for LL chondrites.

Regarding chondrule textural types, a distinction has to be made between specimens 1 and 2. In the first one, the prevalent occurrence of BO and, at a lesser amount, PO and GO chondrules, can be observed; according to some authors (Gooding and Keil 1981; Lauretta et al. 2006), this is not so usual in ordinary chondrites because they are characterized by the following relative abundances porphyritic olivine-pyroxene (POP) >PO>PP>radial pyroxene (RP)>BO. Nevertheless, Hezel et al. (2018), based on literature data for 471 chondrules from several ordinary chondrites, pointed out a different sequence of relative abundances: PO>POP-RP>BO>PP. As concerns specimen 2, although chondrules are generally not well delineated, a more typical distribution has been observed, with prevailing PO chondrules.

But what really gives specimen 1 a distinct character are the modal mineral abundances (Fig. S3 in supporting information) that show significant differences from those reported for other ordinary chondrite meteorites. One of the most intriguing features is the very large amount of olivine (63.1 vol%;

Table 3. Trace element concentration ( $\mu\text{g g}^{-1}$ ).

	Specimen 1	RSD	Specimen 2	RSD
Li	1.47	0.22	2.69	0.34
Sc	11.76	1.53	9.30	1.29
Ti	528.62	0.18	537.39	0.63
V	68.84	0.43	50.75	0.96
Cr	2805.00	0.45	1922.68	0.78
Mn	2827.21	0.79	2652.18	0.32
Co	22.46	0.25	608.34	0.96
Ni	277.26	0.73	13739.70	1.07
Cu	1.50	0.35	94.93	0.63
Zn	57.34	1.94	51.26	0.73
Ga	2.66	0.46	5.05	1.37
Rb	2.73	1.30	3.24	2.40
Sr	13.40	1.16	10.80	2.52
Y	2.94	1.31	1.90	1.83
Zr	8.40	0.49	6.45	0.83
Nb	0.34	1.06	0.42	0.76
Mo	0.05	14.99	0.96	1.01
Sn	0.04	4.48	0.58	2.38
Sb	0.02	5.79	0.07	8.78
Cs	0.05	4.70	0.03	0.69
Ba	3.47	0.79	3.60	1.09
La	0.527	0.688	0.269	1.570
Ce	1.366	0.684	0.696	0.575
Pr	0.198	0.540	0.104	2.518
Nd	0.919	0.372	0.499	0.088
Sm	0.312	0.447	0.175	6.012
Eu	0.100	2.032	0.080	1.539
Gd	0.431	0.840	0.230	2.991
Tb	0.078	0.601	0.044	2.100
Dy	0.505	1.556	0.296	4.191
Ho	0.106	0.704	0.065	1.085
Er	0.288	0.592	0.203	2.500
Yb	0.235	5.707	0.201	4.591
Lu	0.036	1.811	0.032	1.899
Hf	0.192	2.543	0.164	2.842
Ta	0.030	2.583	0.023	2.773
Tl	bdl	85.09	bdl	625.49
Pb	0.242	0.427	0.066	0.599
Th	0.059	2.236	0.044	6.207
U	0.032	0.901	0.014	6.198

RSD is the relative standard deviation of the five individual measurements per element, which are then averaged. Precision and accuracy mentioned in the Techniques and Methods section are based on the reproducibility of the BHVO-2 standard.

67.0 wt%) and extremely low abundance of low-Ca pyroxene (5.8 vol%; 5.8 wt%), as well as the absolute scarcity of iron (kamacite), taenite, and troilite (all together <0.2 wt%). These abundances are surprising considering that Dunn et al. (2010a), using powder X-ray diffraction obtained the following mean values (wt%) for the three groups of ordinary chondrites: olivine (H 29.8–35.7; L 40.7–43.0; LL 49.7–52.5); low-Ca pyroxene (H 27.0–24.9; L 24.2–21.7; LL 22.6–18.9); metal (H 15.3–21.4; L 6.9–9.9; LL 0.5–7.2); troilite (H

4.1–7.0; L 2.6–10.3; LL 3.6–8.6). It is worth mentioning that the abundance of olivine increases from H to LL and, inside each group, usually tends to increase from lower to higher petrologic type so that olivine amount in H4 is less abundant than olivine in H5, and olivine in H5 less abundant than olivine in H6. Conversely the low-Ca pyroxene decreases from H to LL and, inside each group, tends to decrease from lower to higher petrologic type. Finally, the abundance of high-Ca pyroxene varies to a lesser extent among the three groups although tends to show a very slight decrease inside each group.

Even taking into account the maximum abundance of olivine (52.5 wt% in LL6) and the minimum abundance of low-Ca pyroxene (18.9 wt% again in LL6), it is clear that these values are very far from the abundances found in specimen 1. This difference is even more striking if we consider the group and the petrologic type showing the mineral chemistry features that should be close to those present in specimen 1. Thus, Dunn et al. (2010a) suggest that in L5 ordinary chondrites, the olivine abundance is about 42.2 wt% (versus 67.0 wt% in Cavezzo) and the low-Ca pyroxene abundance close to 24.2 wt% (versus 5.8 wt% in Cavezzo). Also considering the results of the study performed by Dunn et al. (2010b), there is a strong discrepancy between the abundance of olivine, orthopyroxene, and clinopyroxene in specimen 1 and the abundances of these minerals in other ordinary chondrites: the ol/(ol+px) ratio in specimen 1 is 0.80 whereas it is at maximum 0.69 for LL (Karatu LL6 chondrite) and 0.61 for L (Kyushu L6 chondrite); the cpx/(opx+cpx) ratio in specimen 1 is 0.64 whereas in the ordinary chondrite, the maximum value 0.34 can be found, by coincidence, in Attarra (L4 chondrite). The unique exception in these abundances is related to the LL6 Saint Séverin where the relative abundances invert to give the following values: low-Ca pyroxene 11 vol% and high-Ca pyroxene 14 vol% (Kovach and Jones 2010).

Although the data of Dunn et al. (2010a, 2010b) were obtained by XRD, it should be underlined that, according to the same authors, the comparison of electron microprobe abundances with XRD abundances appears to suggest that the microprobe phase-mapping technique agrees better with the XRD technique, in particular when the ordinary chondrites become more equilibrated (as in the case of specimen 1). Plagioclase abundance in specimen 1 (18.2 vol%; 14.5 wt%) is slightly higher than the ranges given by Gastineau-Lyons et al. (2002) and Dunn et al. (2010a) for other L chondrites (min 5.7 wt%, max 12.3 wt%).

As concerns phosphates, the mean abundance of chlorapatite in specimen 1a and specimen 1c is 2.1 vol%



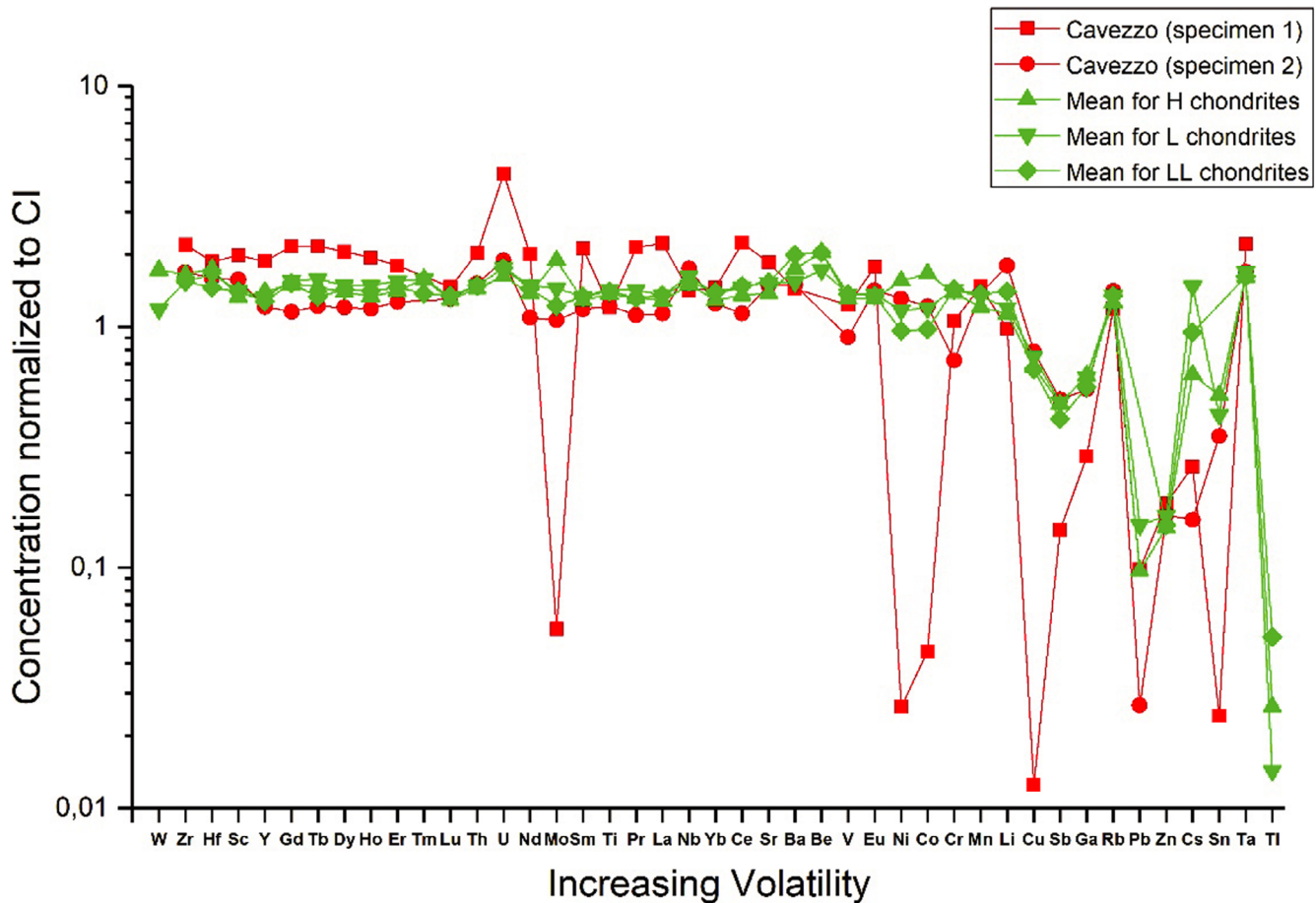


Fig. 9. Cavezzo bulk composition CI-normalized. The pattern for specimen 1 displays significant differences with that for a typical L chondrite composition (Wasson and Kallemeyn 1988; Kallemeyn et al. 1989).

(2.0 wt%) but it goes to 3.1 vol% (2.9 wt%) if only specimen 1 is considered. These values significantly exceed the ones found in other ordinary chondrites. For example, from Gastineau-Lyons et al. (2002) reported values of whitlockite ranging from 0.34 to 0.75 wt%; McSween et al. (1991) normative abundances from 0.29 to 0.79 wt%; Lewis and Jones (2016) abundances from 0.0 to 0.3 vol% in four L chondrites. An exception is the dark fraction of the Saint Séverin LL6 chondrite that contains up to 20 vol% chlorapatite (Crozas and Zinner 1985). Opaque phases also display strong differences when data for the specimen 1 meteorite are compared with those of other ordinary chondrites. The kamacite+taenite (Fe, Ni) abundance in specimen 1 is 0.1 wt% against 0.5 wt% in LL (Benares(a) LL4) to 21.42 wt% in H (Forest Vale H4) but never lower than 5.35 wt% in L chondrites (McSween et al. 1991). Troilite is rare and unquantifiable, as only a single very small grain has been found, whereas in L ordinary chondrites, its abundance ranges from 3.88 wt% (Ramsdorf L6) to 10.3 wt% (Apt L6; McSween et al.

1991; Dunn et al. 2010a). Chromite amounts to 0.5 wt%, a value lower than the range usually observed in ordinary chondrites (min 0.63 wt%, McSween et al. 1991; max 1.15 wt%, Gastineau-Lyons et al. 2002), whereas the abundance of ilmenite 0.1 wt% is in the range of ordinary chondrites (min 0.00, Gastineau-Lyons et al. 2002; max 0.32, McSween et al. 1991).

A completely different situation occurs when specimen 2 is considered because its petrography is more similar to an L chondrite. Chondrules are smaller than in specimen 1 because their size ranges in diameter from 400 to 1500  $\mu\text{m}$  whereas the chondrule types are mainly PO, PP, and BO. This sequence of relative abundances is like that reported for ordinary chondrites (Gooding and Keil 1981; Lauretta et al. 2006). Moreover, the size range is in agreement with the recommended values reported by Friedrich et al. (2015) for L chondrites.

Also, the modal mineralogy of specimen 2 is much more similar to that of ordinary chondrites when compared to specimen 1 (Fig. S3) although some

Table 4. Oxygen isotope composition in Cavezzo meteorite.

Specimen	$\delta^{17}\text{O}\text{‰}$	$1\sigma$	$\delta^{18}\text{O}\text{‰}$	$1\sigma$	$\Delta^{17}\text{O}\text{‰}$	$1\sigma$	$\Delta^{17}\text{O}\text{‰}_{\text{ollinear}}$	1s	1000 ln [1 + ( $\delta^{17}\text{O}_{\text{SMOW}}/$ 1000)]	1000 ln [1 + ( $\delta^{18}\text{O}_{\text{SMOW}}/$ 1000)]
Specimen 1	3.317		4.870		0.785		0.762		3.312	4.858
Specimen 1	3.202		4.648		0.785		0.764		3.197	4.637
Specimen 1	3.232		4.689		0.794		0.772		3.227	4.678
Mean values	3.250	0.060	4.736	0.118	0.788	0.005	0.766	0.005	3.245	4.724
Specimen 2	3.717		4.915		1.161		1.138		3.710	4.903
Specimen 2	3.756		4.999		1.157		1.133		3.749	4.987
Mean values	3.737	0.028	4.957	0.059	1.159	0.003	1.135	0.004	3.730	4.945
Specimen 1	3.268		4.762		0.792		0.770		3.263	4.751
Specimen 1	3.181		4.611		0.783		0.762		3.176	4.600
Mean values	3.225	0.062	4.687	0.107	0.788	0.006	0.766	0.006	3.219	4.676
Specimen 2	3.762		5.003		1.160		1.136		3.755	4.991
Specimen 2	3.748		4.926		1.186		1.163		3.741	4.914
Mean values	3.755	0.010	4.965	0.054	1.173	0.018	1.150	0.019	3.748	4.952

differences may occur. In particular, from a comparison of the values obtained on sample 2a and the values reported by Dunn et al. (2010a) for the L chondrites, the following considerations can be made. Olivine (38.1 wt%) is slightly lower than the lowest value reported for the Bald Mountain meteorite (38.4 wt%); plagioclase (11.0 wt%) is in the range reported from 17 meteorites (7.2–12.3 wt%); high-Ca pyroxene (5.0 wt%) is lower than the lowest value reported for Messina (7.2 wt%); low-Ca pyroxene (27.7 wt%) is a bit higher than the highest value reported for the Blackwell meteorite (25.9 wt%). Phosphate minerals chlorapatite and merrillite are in the range of the abundances reported by Lewis and Jones (2016) for equilibrated L chondrites.

As for opaque phases, chromite abundance (1.3 vol%; 1.6 wt%) is slightly higher than in ordinary chondrite whereas Fe, Ni (4.5 vol%; 9.9 wt%) and troilite (4.8 vol%; 6.3 wt%) are in the range observed for the L chondrites (McSween et al. 1991; Dunn et al. 2010a).

### Crystal Chemistry

In contrast to petrography and modal mineralogy, the compositions of the main and accessory mineral phases in specimen 1 and specimen 2 are quite similar and do not show any substantial difference with those generally observed in ordinary chondrites, in particular those of the L group.

The fayalite content of olivine (Fa 24.6 mol% in specimen 1 and 24.5 mol% in specimen 2) and the ferrosilite content of the low-Ca pyroxene (Fs 20.4 mol% in specimen 1 and 21.0 mol% in specimen 2) plot in the middle of the compositional field for the L chondrite

group (Fig. S4 in supporting information). Even in the diagram CaO, MnO versus FeO, as used by Brearley and Jones (1998), the values of specimen 1 and specimen 2—respectively, <0.05 wt%, 0.47 wt%, 22.62 wt% and <0.05 wt%, 0.47 wt%, and 22.73 are within the L group. Moreover, the very low NiO content (<0.03 wt%) in the olivine indicates that the conditions of formation were not particularly oxidizing, as expected for L chondrites.

Pyroxene, both high-Ca and low-Ca types, displays compositions that are also compatible with literature data for L chondrites. In particular, considering the high-Ca pyroxene, the Fs content (7.79 mol% in specimen 1 and 7.95 mol% in specimen 2) as well as the Wo content (44.23 mol% in specimen 1 and 43.39 in specimen 2) agree well with the values provided by Gastineau-Lyons et al. (2002) for three L group chondrites (namely Bald Mountain, Homestead, and Girgenti). Even minor element concentrations of the high-Ca pyroxene (TiO<sub>2</sub> 0.58 wt%, Al<sub>2</sub>O<sub>3</sub> 0.57 wt%, MnO 0.21 wt%, Cr<sub>2</sub>O<sub>3</sub> 0.88 wt% for specimen 1; TiO<sub>2</sub> 0.45 wt%, Al<sub>2</sub>O<sub>3</sub> 0.48 wt%, MnO 0.21 wt%, Cr<sub>2</sub>O<sub>3</sub> 0.78 wt% for specimen 2) agree with those reported in the diagrams TiO<sub>2</sub>, Al<sub>2</sub>O<sub>3</sub>, Na<sub>2</sub>O versus CaO and MnO, Cr<sub>2</sub>O<sub>3</sub> versus FeO by Brearley and Jones (1998).

The low-Ca pyroxene composition of specimen 1 (Fs 20.41 mol%, Wo 1.40 mol%) and specimen 2 (Fs 20.99 mol%, Wo 1.40) is homogeneous (Fig. S5 in supporting information) and in the range of values provided by Brearley and Jones (1998) and Gastineau-Lyons et al. (2002). Although the contents of Fs and Wo show an approximate increase with the increase of the petrologic type within each chondrite group, we observe that Cavezzo data from both specimens agree better with the values of petrologic type 5 of the L group. It is noteworthy that minor element

concentrations, such as CaO 0.72 wt%, TiO<sub>2</sub> 0.24 wt%, Al<sub>2</sub>O<sub>3</sub> 0.15 wt%, MnO 0.49 wt%, Cr<sub>2</sub>O<sub>3</sub> 0.13 wt% (in specimen 1) and CaO 0.74 wt%, TiO<sub>2</sub> 0.17 wt%, Al<sub>2</sub>O<sub>3</sub> 0.16 wt%, MnO 0.48 wt%, Cr<sub>2</sub>O<sub>3</sub> 0.11 wt% (in specimen 2) fall in the L chondrites field on diagrams of TiO<sub>2</sub>, Al<sub>2</sub>O<sub>3</sub> versus CaO and MnO, Cr<sub>2</sub>O<sub>3</sub> versus FeO (Brearley and Jones 1998).

Compositional analysis of feldspar in specimen 1 and specimen 2 (Fig. S6 in supporting information), although showing slight differences, yields results pointing toward an albitic plagioclase (An 10.82 mol%, Or 5.39 mol% and An 9.76 mol%, Or 5.29 mol%, respectively).

Phosphates, namely chlorapatite in specimen 1 and both chlorapatite + merrillite in specimen 2, show compositions like those reported by Lewis and Jones (2016).

Besides chromite of constant composition, in Cavezzo, there are no traces of Al-rich Cr spinel that occur in many equilibrated ordinary chondrites as large grains in chondrules rich in mesostasis (Wlotzka 2005). Comparing the data with those published by Wlotzka (2005), the mole% Fe/(Fe+Mg) (0.89–0.88) and mole% Cr/Cr+Al (0.88–0.87) ratios of specimen 1 and specimen 2 are compatible both with the values detected in L and LL chondrites.

Iron (*kamacite*) composition in the two specimens is quite different (Table 2). In specimen 1, the Ni content (4.26 wt%) is close to the Ni content occurring in the LL group (4.43–5.47 wt%; Afiattalab and Wasson 1980) whereas in specimen 2, the Ni content (6.12 wt%) is more similar to that found in H group (5.96–6.86 wt%) and L group (5.70–6.67 wt%). As argued by Reisener and Goldstein (2003), *kamacite* Co concentrations vary systematically with respect to chondrite chemical group and, therefore, can be a good indicator to use. Actually, the Co contents in *kamacite* of specimen 1 and specimen 2 (1.59 wt% and 1.18 wt%, respectively) are between those found in L (0.67–0.82 wt%) and LL (2.04–4.60 wt%) groups. As concerns taenite, the Co contents of specimen 1 and specimen 2 are 0.90 wt% and 0.83 wt%, respectively, near to the content reported in the literature for LL chondrites (1.01–0.97 wt%) but different from those of L (mean 0.18 wt%, Afiattalab and Wasson 1980; 0.30 wt%, Kong and Ebihara 1996) and H (0.10 wt%, Afiattalab and Wasson 1980) chondrites.

## Geochemistry

Chemical analyses of minor and trace elements reveal substantial differences between ordinary chondrites and the Cavezzo meteorite (Table 3; Fig. 9). The strong depletion in Mo, Ni, Co, Cu, and Sn and

moderate depletion in Sb, Ga, and Cs of specimen 1 can be justified considering that many of these elements (with the exception of Cs) are siderophile or chalcophile. Therefore, since Fe, Ni metal is exceedingly low and sulfides are basically absent in specimen 1, the abundance of siderophile and chalcophile elements is consequently very low.

Such low abundance of these elements can explain an absolute concentration of the lithophile elements slightly higher than mean L chondrites. According to Mittlefehldt and Lindstrom (2001), this concentration could be consistent with segregation of metal plus troilite (migrated in other portion not present in specimen 1), thus "concentrating" the lithophile elements compared to bulk L chondrites.

As for U, the higher content of specimen 1 (compared to ordinary chondrites) can find an explanation by the presence of a greater amount of chlorapatite that hosts this element.

The strong differences observed in the REEs of specimen 1 and specimen 2 (Fig. 10) confirm that Cavezzo is a "double face" meteorite. Complementary correlation, as soon as the opposite Eu anomalies (negative in specimen 1 and positive in specimen 2), is not unusual in meteorites (Masuda et al. 1973; Dauphas and Pourmand 2015) but not in the same meteorite. Hence, the differences are related to the different modal mineralogy of the two specimens and, in particular, to a dissimilar content of Ca-phosphate, Ca-pyroxene, and plagioclase.

## Oxygen Isotopes

On a diagram of  $\delta^{17}\text{O}$  versus  $\delta^{18}\text{O}$  (Fig. 11), specimen 1 plots on the boundary between the H and L groups, whereas specimen 2 plots along the boundary between the L and LL groups. These data suggest that specimen 1 is derived from isotopically distinct material compared to that of specimen 2. Xenoliths of one type of ordinary chondrite within an isotopically distinct ordinary chondrite host have been documented in many other meteorites (e.g., Bridges and Hutchison 1997; Herd et al. 2013; Ruzicka et al. 2019). The evidence from oxygen isotope analysis suggests that specimen 1, at least in part, consists of "xenolithic" material, with specimen 2 representing the enclosing host material.

## Classification

### Class and Group

Specimen 1 is undoubtedly an equilibrated ordinary chondrite-related sample although it also appears to show a number of unique characteristics. There is a clear ambiguity when comparing the classification information provided by oxygen isotopes, olivine, and

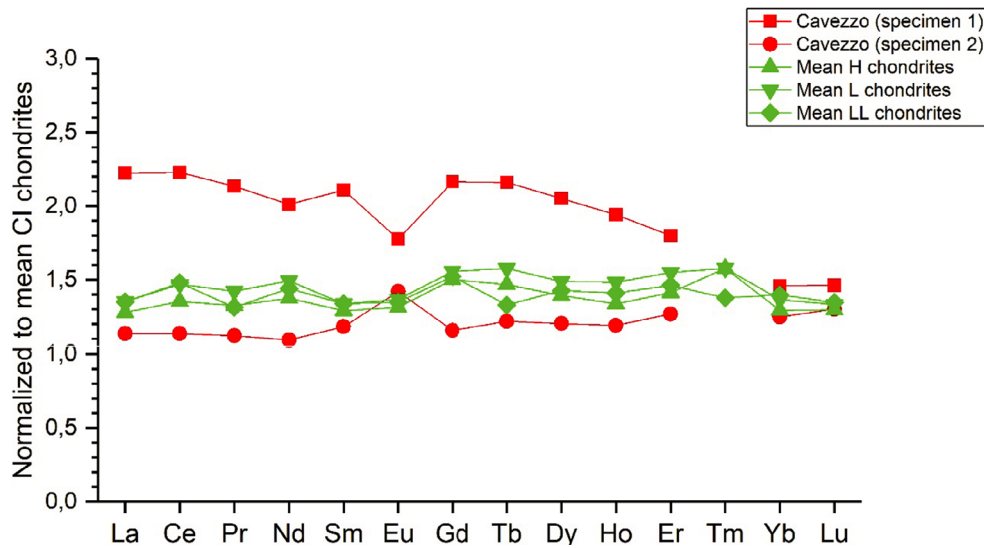


Fig. 10. REE pattern of specimen 1 and specimen 2 compared to those of ordinary chondrites. It is noteworthy that LREE and HREE of specimen 1 decrease whereas LREE and HREE of specimen 2 increase. Data for H, L, LL chondrites from Wasson and Kallemeyn (1988) and Kallemeyn et al. (1989).

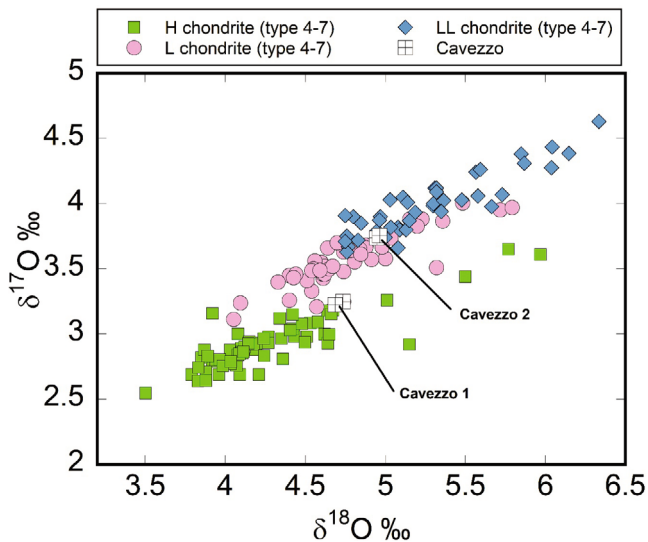


Fig. 11. Oxygen isotopes composition of Cavezzo: specimen 1 plots at the junction between the H and L fields whereas specimen 2 plots at the boundary between L and LL fields (Data: Clayton et al. [1991] and Meteoritical Bulletin Database)

low-Ca pyroxene compositions (that are typical of L-chondrite group) on the one hand and the mineralogical modal abundances on the other. Both specimen 1 and specimen 2 show mean composition for olivine and low-Ca pyroxene which are within expected values of Fa 22.7–25.6 (mean Fa 24.6) and Fs 18.7–22.6 (mean Fs 21.3) for L group chondrites. Furthermore, the average plagioclase composition for specimen 1 and specimen 2

is also very close to the average plagioclase composition (An 10.2, Or 5.6) for L chondrites. Even more importantly, the oxygen isotopes, although different between them (Fig. 11), plot in the L field of the ordinary chondrites. In specimen 1, the very low amount of metal, the absolute scarcity of sulfides, and the high-Ca pyroxene/(high-Ca pyroxene + low-Ca pyroxene) ratio point toward an LL group composition. This is the reason why specimen 1 has to be recognized as an anomalous member of the L-chondrite group. As discussed earlier, the oxygen isotope composition of specimens 1 and 2 are consistent with a xenolith–host relationship.

#### *Petrologic Type*

Although in both specimen 1 and specimen 2 olivine, pyroxenes and plagioclase compositions plot in tight clusters and distinct groups (Figs. S4–S6)—all of which are characteristics indicative of a high petrological type ( $\geq 5$ ) with an advanced degree of chemical equilibration—the size of plagioclase ( $< 50 \mu\text{m}$ ) and the CaO content in orthopyroxene suggest a petrological type 5 (Van Schmus and Wood 1967; Tait et al. 2014). Nevertheless, it is worth noting that in specimen 1, matrix has completely recrystallized into a coarser texture but some chondrules are still well delineated; specimen 2 has a fine-grained matrix with relics and not so clearly delineated chondrules.

#### *Weathering Grade and Shock Stage*

Specimen 1 is a fall and, just like the main mass (specimen 2), was recovered and collected within 4 days

of its fall. Therefore, neither primary nor secondary weathering has developed, and the weathering grade is W0 according to the proposed weathering scale (Wlotzka 1993; Wlotzka et al. 1995; Al-Kathiri et al. 2005; Zurfluh et al. 2016).

Despite the intensive fracturing of the olivine and other minerals that are pervasive in the samples, all grains show a sharp optical extinction without any trace of undulatory extinction. These parameters indicate a shock stage of S1 according to the scheme of Stöffler et al. (1991). Nevertheless, in specimen 1, some plagioclase–chromite assemblages occur (Fig. 7h) along with chromite veinlets in olivine crystals (Figs. 7a and 7b). These features have been reported in some ordinary chondrites that experienced shock heating (Dodd and Jarosewich 1982; Xie et al. 2001; Rubin 2003), indicating that the intergrowths themselves could be the result of shock-induced melting.

Therefore, following Rubin (2003), it could be assumed that specimen 1 was shocked to levels of at least shock-stage S3 and then subject to a postshock annealing that resets the shock stage to S1, yielding a sharp optical extinction. However, if this scenario were true, it would be difficult to explain the presence of unmelted chromite grains in the plagioclase as well as the lack of other evidence, such as extensive silicate darkening, myrmekitic plessite, and a relatively high abundance of metallic Cu (Rubin 2003).

Specimen 2 shows no evidence of shock nor does the occurrence of particular mineralogical assemblage. Nevertheless, a heating that obliterated the evidence of a previous shock event cannot be excluded.

### *An Anomalous L-Chondrite*

Cavezzo is a “double-faced” meteorite because the two specimens have clearly distinct characteristics. Indeed, not only are they easily distinguishable on the basis of modal mineralogy and texture but also the oxygen isotopes, which fall at the extremes of the L chondrite field (Fig. 11), confirm that they are two different meteorites. However, while specimen 2 shows characteristics typical of usual ordinary chondrites, specimen 1 has a modal mineralogy (high abundance of olivine and low abundance of low-Ca pyroxene) and texture (from chondritic to “achondritic”) that are completely anomalous for a chondrite.

Some of the characteristics of specimen 1 might resemble those of shock melted and recrystallized chondrites (Saint Severin, Chico, DaG 896, etc.) whose real nature could not be immediately recognized due to the appearance of an achondritic texture. As an example, DaG 896 was initially mistaken for an achondrite (Folco et al. 2004) and only successively was recognized by the same authors as an H-impact melt.

These meteorites may also reveal residual chondrules within the shocked clasts and metal–sulfide depletion. Moreover, the shocked melted and recrystallized meteorites often present brecciated structures, impact melts clearly visible as glasses and residual chondritic clasts well distinct from the melt (see Bogard et al. [1995] for the Chico meteorite). Furthermore, the composition of the recrystallized pyroxene may be highly variable, as occurs in Patuxent Range 91501 (Mittlefehldt and Lindstrom 2001) and in DaG 896 (Folco et al. 2004).

As a matter of fact, specimen 1 does not show any of these characteristics. There is no evidence of glass, clastic, or brecciated texture like those observed by Friedrich et al. (2014). In the low-Ca pyroxenes, there is no positive linear correlation between  $\text{TiO}_2$  and  $\text{Al}_2\text{O}_3$  that is indicative of igneous fractionation and has been observed both in Patuxent Range 91501 (Mittlefehldt and Lindstrom 2001) and in DaG 896. Furthermore, specimen 1 can be neither a unique mega-chondrule like those found in some meteorites (Ruzicka et al. 1998), because specimen 1 contains some clearly distinguished chondrules, nor, for the same reason, a recrystallized portion of an impact melt pocket.

Although specimen 1 presents in some portions an overall igneous texture, it is difficult to justify this characteristic in a framework of recrystallization from shock melt because, if this were true, the equilibrated crystal chemistry of specimen 1’s mineral phases would have required a more protracted crystallization interval. Such crystallization is not easily explained in the light of well-formed chondrules that are intermingled with the igneous texture.

In conclusion, given the differences between the two Cavezzo specimens in terms of oxygen isotopes, modal mineralogy, and texture, specimen 1 is a “xenolith” and not a recrystallized melt pocket. However, specimen 1 remains anomalous because it cannot simply represent a recrystallized melt clast, considering that its chondrules are intermingled with large crystals of olivine and a gradual transition to the “achondritic” portion of the specimen can be observed (Figs. 2, 3, and S7).

## CONCLUSIONS

Both Cavezzo specimens belong to the chondritic class, as shown by the occurrence of chondrules, and are characterized by the identical composition of the main and secondary phases. The composition of olivine, low-Ca and high-Ca pyroxene, and plagioclase is very similar in both specimens—and these compositions tend to match the compositional fields of the ordinary L-group chondrites. Despite these similarities, specimen 1 and specimen 2 are different because of their textural

features, modal mineralogy, geochemistry, and oxygen isotopic composition.

Some of these characteristics, while not anomalous for ordinary chondrites overall, can be useful to distinguish specimen 1 from specimen 2. For example, specimen 1 is characterized by a very low amount of Fe, Ni metal and sulfides (much lower than LL chondrites) whereas in specimen 2, their amount is compatible with L chondrites. Specimen 1 contains chlorapatite whereas specimen 2 contains both chlorapatite and merrillite. Specimen 1 shows the occurrence of spinel within the plagioclase veins whereas specimen 2 does not show this feature. It is noteworthy that the oxygen isotope compositions of the two specimens, although both plot in the L-chondrite field, are clearly different from each other.

Other characteristics are not only peculiar to specimen 1 but are also distinctive with respect to the other ordinary chondrites known so far. In fact, specimen 1 presents large chondrules and large crystals in the matrix that are not limited to silicates but likewise concern phosphate (i.e., chlorapatite). Moreover, there are aspects related to the large amount of olivine (very high ol/ol+px ratio) and to the anomalous ratio of low-Ca and high-Ca pyroxenes (high cpx/cpx+opx ratio).

The geochemistry of the Cavezzo meteorite is then quite intriguing because in specimen 1, the concentration of almost all elements, except siderophiles and chalcophiles that are strongly depleted, is slightly enriched compared to that of ordinary chondrites. Furthermore, specimen 1 and specimen 2 have very dissimilar REE patterns from each other.

These characteristics, considering that specimen 1 shows no portions similar to specimen 2 and vice versa, prevent the Cavezzo meteorite from being classified as a breccia. In conclusion, by virtue of the peculiarities of specimen 1, this fall has to be classified as an anomalous L5 ordinary chondrite where specimen 1 is a “xenolith” that might represent a previously unsampled portion of the L chondrite parent body.

*Acknowledgments*—PRISMA is the Italian Network for Systematic Surveillance of Meteors and Atmosphere. It is a collaboration initiated and coordinated by the Italian National Institute for Astrophysics (INAF) that counts members among research institutes, associations, and schools. The complete list of PRISMA members is available here: <http://www.prisma.inaf.it>. PRISMA was partially funded by 2016/0476 and 2019/0672 Research and Education grants from “Fondazione Cassa di Risparmio di Torino” and by a 2016 grant from “Fondazione Agostino De Mari” (Savona). PRISMA data are hosted and made available to the public by the INAF research e-infrastructure project IA2 (Italian

Center for Astronomical Archives). The authors are grateful to INAF and all supporters of the PRISMA network. Thanks to their efforts, in fact, it was possible not only to trace and study the trajectory of the bolide but also to find the meteorite.

We would especially like to thank A. J. Timothy Jull and Luigi Folco for their support and constructive discussions on this matter.

We would also like to show our gratitude to Mr. Gaddi who decided to donate the meteorite to the INAF. Thanks to Dr. Giulia Degli Alessandrini (Open University), Dr. Andrea Orlando, and Dr. Eleonora Braschi (IGG-CNR), who supported us for WDS. Thanks to Dr. Laura Chiarantini (MEMA—Università di Firenze) for EDS analyses. Oxygen isotope studies at the Open University are funded by a consolidated grant from the Science and Technology Facilities Council (STFC), UK.

*Data Availability Statement*—Data openly available in a public repository that issues data sets with DOIs.

*Editorial Handling*—Dr. Timothy Jull

## REFERENCES

- Afiatalab F. and Wasson J. T. 1980. Composition of the metal phase in ordinary chondrites: Implications regarding classification and metamorphism. *Geochimica et Cosmochimica Acta* 44:431–446.
- Al-Kathiri A., Hofmann B. A., Jull A. J. T., and Gnos E. 2005. Weathering of meteorites from Oman: Correlation of chemical and mineralogical weathering proxies with <sup>14</sup>C terrestrial ages and the influence of soil chemistry. *Meteoritics & Planetary Science* 40:1215–1239.
- Barghini D., Gardiol D., Carbognani A., and Mancuso S. 2019. Astrometric calibration for all-sky cameras revisited. *Astronomy & Astrophysics* 626:A105.
- Benedix G. K., Bland P. A., Friedrich J. M., Mittlefehldt D. W., Sanborn M. E., Yin Q.-Z., Greenwood R. C., Franchi I. A., Bevan A. W. R., Towner M. C., Perrotta G. C., and Mertzman S. A. 2017a. Bunburra Rockhole: Exploring the geology of a new differentiated asteroid. *Geochimica et Cosmochimica Acta* 208:145–159.
- Benedix G. K., Forman L. V., Daly L., Godel B., Esteban L., Meier M. M. M., Maden C., Busemann H., Yin Q.-Z., Sanborn M. E., Ziegler K., Strasser J. W., Welten K. C., Caffee M. W., Glavin D. P., Dworkin J. P., Bland P. A., Paxman J. P., Towner M. C., Cupak M., Sansom E. K., Howie R. M., Devillepoix H. A. R., Cox M. A., Jansen-Sturgeon T., Hartig B. A. D., and Bevan A. W. 2017b. Mineralogy, petrology and chronology of the Dingle Dell meteorite. 80th Annual Meeting of the Meteoritical Society. Paper 6229.
- Bischoff A., Barrat J.-A., Bauer K., Burkhardt C., Busemann H., Ebert S., Gonsior M., Hakenmüller J., Haloda J., Harries D., Heinlein D., Hiesinger H., Hochleitner R., Hoffmann V., Kaliwoda M., Laubenstein M., Maden C., Meier M. M. M., Morlok A., Pack A., Ruf A., Schmitt-Kopplin P., Schönbächler M., Steele R. C. J., Spurný P.,

- and Wimmer K. 2017. The Stubenberg meteorite—An LL6 chondrite fragmental breccia recovered soon after precise prediction of the strewn field. *Meteoritics & Planetary Science* 52:1683–1703.
- Bland P. A., Spurny P., Towner M. C., Bevan A. W. R., Singleton A. T., Bottke W. F., Greenwood R. C., Chesley S. R., Shrubny L., Borovicka J., Ceplecha Z., McClafferty T. P., Vaughan D., Benedix G. K., Deacon G., Howard K. T., Franchi I. A., and Hough R. M. 2009. An anomalous basaltic meteorite from the innermost main belt. *Science* 325:1525–1527.
- Bland P. A., Towner M. C., Sansom E. K., Devillepoix H., Howie R. M., Paxman J. P., Cupak M., Benedix G. K., Cox M. A., Jansen-Sturgeon T., Stuart D., and Strangeway D. 2016. Fall and recovery of the Murrili meteorite and an update on the Desert Fireball Network. 79th Annual Meeting of the Meteoritical Society. Paper 6265.
- Bogard D. D., Garrison D. H., Norman M., Scott E. R. D., and Keil K. 1995.  $^{39}\text{Ar}$ - $^{40}\text{Ar}$  age and petrology of Chico: Large-scale impact melting on the L-chondrite parent body. *Geochimica et Cosmochimica Acta* 59:1383–1399.
- Brearley A. J. and Jones R. H. 1998. Chondritic meteorites. In *Planetary materials*, edited by Papike J. J. Reviews in Mineralogy, vol. 36. Washington, D.C.: Mineralogical Society of America. pp. 3-1–3-98.
- Bridges J. C. and Hutchison R. 1997. A survey of clasts and large chondrules in ordinary chondrites. *Meteoritics & Planetary Science* 32:389–394.
- Carbognani A., Barghini D., Gardiol D., Martino M. D., Valsecchi G. B., Trivero P., Buzzoni A., Rasetti S., Selvestrel D., Knapic C., Londero E., Zorba S., Volpicelli C. A., Carlo M. D., Vaubaillon J., Marmo C., Colas F., Valeri D., Zanotti F., Morini M., Demaria P., Zanda B., Bouley S., Vernazza P., Gattacceca J., Rault J. L., Maquet L., and Birlan M. 2020. A case study of the May 30, 2017, Italian fireball. *European Physical Journal Plus* 135:255.
- Ceplecha Z. 1961. Multiple fall of Příbram meteorites photographed. *Bulletin Astronomical Institute Czechoslovakia* 12:21–47.
- Clayton R. N., Mayeda T. K., Goswami J. N., and Olsen E. J. 1991. Oxygen isotope studies of ordinary chondrites. *Geochimica et Cosmochimica Acta* 55:2317–2337.
- Colas F., Zanda B., Bouley S., Jeanne S., Maltgoyre A., Birlan M., Blanpain C., Gattacceca J., Jorda L., Lecubin J., Marmo C., Rault J. L., Vaubaillon J., Vernazza P., Yohia C., Gardiol D., Nedelcu A., Poppe B., Rowe J., Forcier M., Koschny D., Trigo-Rodriguez J. M., Lamy H., Behrend R., Ferrière L., Barghini D., Buzzoni A., Carbognani A., Di Carlo M., Di Martino M., Knapic C., Londero E., Pratesi G., Rasetti S., Riva W., Stirpe G. M., Valsecchi G. B., Volpicelli C. A., Zorba S., Coward D., Drolshagen E., Drolshagen G., Hernandez O., Jehin E., Jobin M., King A., Nitschelm C., Ott T., Sanchez-Lavega A., Toni A., Abraham P., Affaticati F., Albani M., Andreis A., Andrieu T., Anghel S., Antaluca E., Antier K., Appéré T., Armand A., Ascione G., Audureau Y., Auxepales G., Avoscan T., Baba A. D., Bacci P., Bădescu O., Baldini R., Baldo R., Balestrero A., Baratoux D., Barbotin E., Bardy M., Basso S., Bautista O., Bayle L. D., Beck P., Bellitto R., Belluso R., Benna C., Benammi M., Beneteau E., Benkhaldoun Z., Bergamini P., Bernardi F., Bertaina M. E., Bessin P., Betti L., Bettonvil F., Bihel D., Birnbaum C., Blagoi O., Blouri E., Boacă I., Boată R., Bobiet B., Bonino R., Boros K., Bouchet E., Borgeot V., Bouchez E., Boust D., Boudon V., Bouman T., Bourget P., Brandenburg S., Bramond P. H., Braun E., Bussi A., Cacault P., Caillier B., Calegari A., Camargo J., Caminade S., Campana A. P. C., Campbell-Burns P., Canal-Domingo R., Carell O., Carreau S., Cascone E., Cattaneo C., Cauhape P., Cavier P., Celestin S., Cellino A., Champenois M., Chennaoui Aoudjehane H., Chevrier S., Cholvy P., Chomier L., Christou A., Cricchio D., Coadou P., Coccagn J. Y., Cochard F., Cointin S., Colombi E., Colque Saavedra J. P., Corp L., Costa M., Costard F., Cottier M., Cournoyer P., Coustal E., Cremonese G., Cristea O., Cuzon J. C., D'Agostino G., Daifallah K., Dănescu C., Dardon A., Dasse T., Davadan C., Debs V., Defaix J. P., Deleflie F., D'Elia M., De Luca P., De Maria P., Deverchère P., Devillepoix H., Dias A., Di Dato A., Di Luca R., Dominici F. M., Drouard A., Dumont J. L., Dupouy P., Duvignac L., Egal A., Erasmus N., Esseiva N., Ebel A., Eisengarten B., Federici F., Feral S., Ferrant G., Ferreol E., Finitzer P., Foucault A., Francois P., Frincu M., Froger J. L., Gaborit F., Gagliarducci V., Galard J., Gardavot A., Garmier M., Garnung M., Gautier B., Gendre B., Gerard D., Gerardi A., Godet J. P., Grandchamps A., Grouiez B., Groult S., Guidetti D., Giuli G., Hello Y., Henry X., Herbreteau G., Herpin M., Hewins P., Hillairiet J. J., Horak J., Hueso R., Huet E., Huet S., Hyaumé F., Interrante G., Isselin Y., Jeangeorges Y., Janeux P., Jeanneret P., Jobse K., Jouin S., Jouvard J. M., Joy K., Julien J. F., Kacerek R., Kaïre M., Kempf M., Koschny D., Krier C., Kwon M. K., Lacassagne L., Lachat D., Lagain A., Laisné E., Lanchares V., Laskar J., Lazzarin M., Leblanc M., Lebreton J. P., Lecomte J., Le Dû P., Lelong F., Lera S., Leoni J. F., Le-Pichon A., Le-Poupon P., Leroy A., Leto G., Levansuu A., Lewin E., Lienard A., Licchelli D., Locatelli H., Loehle S., Loizeau D., Luciani L., Maignan M., Manca F., Mancuso S., Mandon E., Mangold N., Mannucci F., Maquet L., Marant D., Marchal Y., Marin J. L., Martin-Brisset J. C., Martin D., Mathieu D., Maury A., Mespoulet N., Meyer F., Meyer J. Y., Meza E., Moggi Cecchi V., Moiroud J. J., Millan M., Montesarchio M., Misiano A., Molinari E., Molau S., Monari J., Monflier B., Monkos A., Montemaggi M., Monti G., Moreau R., Morin J., Mourgues R., Mousis O., Nablan C., Nastasi A., Niacșu L., Notez P., Ory M., Pace E., Paganelli M. A., Pagola A., Pajuelo M., Palacián J. F., Pallier G., Paraschiv P., Pardini R., Pavone M., Pavy G., Payen G., Pegoraro A., Peña-Asensio E., Perez L., Pérez-Hoyos S., Perlerin V., Peyrot A., Peth F., Pic V., Pietronave S., Pilger C., Piquel M., Pisanu T., Poppe M., Portois L., Prezeau J. F., Pugno N., Quantin C., Quitté G., Rambaux N., Ravier E., Repetti U., Ribas S., Richard C., Richard D., Rigoni M., Rivet J. P., Rizzi N., Rochain S., Rojas J. F., Romeo M., Rotaru M., Rotger M., Rougier P., Rousselot P., Rousset J., Rousseu D., Rubiera O., Rudawska R., Rudelle J., Ruguet J. P., Russo P., Sales S., Sauzereau O., Salvati F., Schieffer M., Schreiner D., Scribano Y., Selvestrel D., Serra R., Shengold L., Shuttleworth A., Smareglia R., Sohy S., Soldi M., Stanga R., Steinhauser A., Straffella F., Sylla Mbaye S., Smedley A. R. D., Tagger M., Tanga P., Taricco C., Teng J. P., Tercu J. O., Thizy O., Thomas J. P., Tombelli M., Trangosi R., Tregon B., Trivero P., Tukkers A., Turcu V., Umbriaco G., Unda-Sanzana E., Vairetti R., Valenzuela

- M., Valente G., Varennes G., Vauclair S., Vergne J., Verlinden M., Vidal-Alaiz M., Vieira-Martins R., Viel A., Vintdevară D. C., Vinogradoff V., Volpini P., Wendling M., Wilhelm P., Wohlgemuth K., Yanguas P., Zagarella R., and Zollo A. 2020. FRIPON: A worldwide network to track incoming meteoroids. *Astronomy & Astrophysics* 644:23.
- Colombetti P., Taricco C., Bhandari N., Sinha N., Di Martino M., Cora A., and Vivaldo G. 2013. Low  $\gamma$  activity measurement of meteorites using HPGe–NaI detector system. *Nuclear Instruments and Methods in Physics Research A* 718:140–142.
- Crozaz G. and Zinner E. 1985. Ion probe determinations of the rare earth concentrations of individual meteoritic phosphate grains. *Earth and Planetary Science Letters* 73:41–52.
- Dauphas N. and Pourmand A. 2015. Thulium anomalies and rare earth element patterns in meteorites and Earth: Nebular fractionation and the nugget effect. *Geochimica et Cosmochimica Acta* 163:234–261.
- Dodd R. T. and Jarosewich E. 1982. The compositions of incipient shock melts in L6 chondrites. *Earth and Planetary Science Letters* 59:355–363.
- Dunn T. L., Cressley G., McSween H. Y. Jr., and McCoy T. J. 2010a. Analysis of ordinary chondrites using powder X-ray diffraction: 1. Modal mineral abundances. *Meteoritics & Planetary Science* 45:123–134.
- Dunn T. L., McCoy T. J., Sunshine J. M., and McSween H. Y. Jr. 2010b. A coordinated spectral, mineralogical, and compositional study of ordinary chondrites. *Icarus* 208:789–797.
- Dyl K. A., Benedix G. K., Bland P. A., Friedrich J. M., Spurný P., Towner M. C., Claire O. K. M., Howard K., Greenwood R., Macke R. J., Britt D. T., Halfpenny A., Thostenson J. O., Rudolph R. A., Rivers M. L., and Bevan A. W. R. 2016. Characterization of Mason Gully (H5): The second recovered fall from the Desert Fireball Network. *Meteoritics & Planetary Science* 51:596–613.
- Folco L., Bland P. A., D’Orazio M., Franchi I. A., Kelley S. P., and Rocchi S. 2004. Extensive impact melting on the H-chondrite parent asteroid during the cataclysmic bombardment of the early solar system: Evidence from the achondritic meteorite Dar al Gani 896. *Geochimica et Cosmochimica Acta* 68:2379–2397.
- Franza A. and Pratesi G. 2021a. Meteorites as a scientific heritage. *Conservar Patrimonio* 36:106–121.
- Franza A. and Pratesi G. 2021b. Mineralogical, petrological and planetological heritage. The (Italian) story so far. *Rendiconti Lincei* 32:95–116.
- Friedrich J. M., Perrotta G. C., and Kimura M. 2014. Compositions, geochemistry, and shock histories of recrystallized LL chondrites. *Geochimica et Cosmochimica Acta* 139:83–97.
- Friedrich J. M., Weisberg M. K., Ebel D. S., Biltz A. E., Corbett B. M., Iotzov I. V., Khan W. S., and Wolman M. D. 2015. Chondrule size and related physical properties: A compilation and evaluation of current data across all meteorite groups. *Chemie der Erde—Geochemistry* 75:419–443.
- Gardiol D. and the PRISMA-Team. 2019. News from the Italian PRISMA fireball network. pp. 81–86. Proceedings of the 37th International Meteor Conference, Pezinok-Modra, Slovakia, August 30–September 2, 2018. pp. 81–86.
- Gardiol D., Barghini D., Buzzoni A., Carbognani A., Di Carlo M., Di Martino M., Knapic C., Londero E., Pratesi G., Rasetti S., Riva W., Salerno R., Stirpe G., Valsecchi G., Volpicelli C., Zorba S., Colas F., Zanda B., Bouley S., Jeanne S., Malgoyre A., Birlan M., Blanpain C., Gattacceca J., Lecubin J., Marmo C., Rault J., Vaubaillon J., Vernazza P., Affaticati F., Albani M., Andreis A., Ascione G., Avoscan T., Bacci P., Baldini R., Balestrero A., Basso S., Bellitto R., Belluso M., Benna C., Bernardi F., Bertaina M. E., Betti L., Bonino R., Boros K., Bussi A., Carli C., Carriero T., Cascone E., Cattaneo C., Cellino A., Colombetti P., Colombi E., Costa M., Cremonese G., Cricchio D., D’Agostino G., D’Elia M., De Maio M., Demaria P., Di Dato A., Di Luca R., Federici F., Gagliarducci V., Gerardi A., Giuli G., Guidetti D., Interrante G., Lazzarin M., Lera S., Leto G., Licchelli D., Lippolis F., Manca F., Mancuso S., Mannucci F., Masi R., Masiero S., Meucci S., Misiano A., Moggi C. V., Molinari E., Monari J., Montemaggi M., Montesarchio M., Monti G., Morini P., Nastasi A., Pace E., Pardini R., Pavone M., Pegoraro A., Pietronave S., Pisanu T., Pugno N., Repetti U., Rigoni M., Rizzi N., Romeni G., Romeo M., Rubineti S., Russo P., Salvati F., Selvestrel D., Serra R., Simoncelli C., Smareglia R., Soldi M., Stanga R., Strafella F., Suvieri M., Taricco C., Tigani S. G., Tombelli M., Trivero P., Umbriaco G., Vairetti R., Valente G., Volpini P., Zagarella R., and Zollo A. 2021. Cavezzo, the first Italian meteorite recovered by the PRISMA fireball network. Orbit, trajectory, and strewn-field. *Monthly Notices of the Royal Astronomical Society* 501:1215–1227.
- Gastineau-Lyons H. K., McSween H. Y. Jr., and Gaffey M. J. 2002. A critical evaluation of oxidation versus reduction during metamorphism of L and LL group chondrites, and implications for asteroid spectroscopy. *Meteoritics & Planetary Science* 37:75–89.
- Gattacceca J., McCubbin F. M., Bouvier A., and Grossman J. N. 2021. The Meteoritical Bulletin No. 109. *Meteoritics & Planetary Science*. in press.
- Gooding J. L. and Keil K. 1981. Relative abundances of chondrule primary textural types in ordinary chondrites and their bearing on conditions of chondrule formation. *Meteoritics* 16:17–43.
- Grady M. M., Pratesi G., and Moggi C. V. 2014. *Atlas of meteorites*. Cambridge: Cambridge University Press. 384 p.
- Granvik M. and Brown P. 2018. Identification of meteorite source regions in the solar system. *Icarus* 311:271–287.
- Greenwood R. C., Burbine T. H., Miller M. F., and Franchi I. A. 2017. Melting and differentiation of early-formed asteroids: The perspective from high precision oxygen isotope studies. *Chemie der Erde* 27:1–43.
- Herd C. D. K., Friedrich J. M., Greenwood R. C., and Franchi I. A. 2013. An igneous-textured clast in the Peace River meteorite: Insights into accretion and metamorphism of asteroids in the early solar system. *Canadian Journal of Earth Sciences* 50:14–25.
- Hezel D. C., Harak M., and Libourel G. 2018. What we know about elemental bulk chondrule and matrix compositions: Presenting the ChondriteDB Database. *Chemie der Erde* 78:1–14.
- Jenniskens P., Rubin A. E., Yin Q.-Z., Sears D. W. G., Sandford S. A., Zolensky M. E., Krot A. N., Blair L., Kane D., Utas J., Verish R., Friedrich J. M., Wimpenny J., Eppich G. R., Ziegler K., Verosub K. L., Rowland D. J., Albers J., Gural P. S., Grigsby B., Fries M. D., Matson



- R., Johnston M., Silber E., Brown P., Yamakawa A., Sanborn M. E., Laubenstein M., Welten K. C., Nishiizumi K., Meier M. M. M., Busemann H., Clay P., Caffee M. W., Schmitt-Kopplin P., Hertkorn N., Glavin D. P., Callahan M. P., Dworkin J. P., Wu Q., Zare R. N., Grady M., Verchovsky S., Emel'Yanenko V., Naroenkov S., Clark D. L., Girten B., Worden P. S., and Consortium T. N. M. 2014. Fall, recovery, and characterization of the Novato L6 chondrite breccia. *Meteoritics & Planetary Science* 49:1388–1425.
- Jenniskens P., Utas J., Yin Q.-Z., Matson R. D., Fries M., Howell J. A., Free D., Albers J., Devillepoix H., Bland P., Miller A., Verish R., Garvie L. A. J., Zolensky M. E., Ziegler K., Sandborn M. E., Versoub K. L., Rowland D. J., Ostrowski D. R., Bryson K., Laubenstein M., Zhou Q., Li Q.-L., Li X.-H., Liu Y., Tang G.-Q., Welten K., Caffee M. W., Meier M. M. M., Planet A., Maden C., Busemann H., and Granvik M. 2019. The Creston, California meteorite fall and the origin of L chondrites. *Meteoritics & Planetary Science* 54:699–720.
- Jenniskens P., Moskovitz N., Garvie L. A. J., Yin Q.-Z., Howell J. A., Free D. L., Albers J., Samuels D., Fries M. D., Mane P., Dunlap D. R., Ziegler K., Sanborn M. E., Zhou Q., Li Q.-L., Li H.-X., Liu Y., Tang G.-Q., Welten K. C., Caffee M. W., Busemann H., Meier M. M. M., and Nesvorný D. 2020. Orbit and origin of the LL7 chondrite Dishchii'bi'koh (Arizona). *Meteoritics & Planetary Science* 55:535–557.
- Kalašová D., Zikmund T., Spurný P., Haloda J., Borovička J., and Kaiser J. 2020. Chemical and physical properties of Žďár nad Sázavou L chondrite and porosity differentiation using computed tomography. *Meteoritics & Planetary Science* 55:1073–1081.
- Kallemeyn G. W., Rubin A. E., Wand D., and Wasson J. T. 1989. Ordinary chondrites. Bulk compositions, classification, lithophile element fractionations, and composition-petrographic type relationships. *Geochimica et Cosmochimica Acta* 53:2747–2767.
- Kong P. and Ebihara M. 1996. Metal phases of L chondrites: Their formation and evolution in the nebula and in the parent body. *Geochimica et Cosmochimica Acta* 60:2667–2680.
- Kovach H. A. and Jones R. J. 2010. Feldspar in type 4–6 ordinary chondrites: Metamorphic processing on the H and LL chondrite parent bodies. *Meteoritics & Planetary Science* 45:246–264.
- Lauretta D. S., Nagahara H., and Alexander C. M. O'D. 2006. Petrology and origin of ferromagnesian silicate chondrules. In *Meteorites and the early solar system II*, edited by Lauretta D. S. and McSween H. Y. Tucson, Arizona: The University of Arizona Press. pp. 431–459.
- Lewis J. A. and Jones R. J. 2016. Phosphate and feldspar mineralogy of equilibrated L chondrites: The record of metasomatism during metamorphism in ordinary chondrite parent bodies. *Meteoritics & Planetary Science* 51:1886–1913.
- Masuda A., Nakamura N., and Tanaka T. 1973. Fine structures of mutually normalized rare-earth patterns of chondrites. *Geochimica et Cosmochimica Acta* 37:239–248.
- McSween H. Y. Jr., Bennett M. E., and Jarosewich E. 1991. The mineralogy of ordinary chondrites and implications for asteroid spectrophotometry. *Icarus* 90:107–116.
- Miller M. F., Franchi I. A., Sexton A. S., and Pillinger C. T. 1999. High precision  $\delta^{17}\text{O}$  isotope measurements of oxygen from silicates and other oxides: Method and applications. *Rapid Communications in Mass Spectrometry* 13:1211–1217.
- Mittlefehldt D. W. and Lindstrom M. M. 2001. Petrology and geochemistry of Patuxent Range 91501, a clast-poor impact melt from the L-chondrite parent body and Lewis Cliff 88663, an L7 chondrite. *Meteoritics & Planetary Science* 36:439–457.
- Reisener R. J. and Goldstein J. I. 2003. Ordinary chondrite metallography: Part 2. Formation of zoned and unzoned metal particles in relatively unshocked H, L and LL chondrites. *Meteoritics & Planetary Science* 38:1679–1696.
- Rubin A. E. 1997. Mineralogy of meteorite groups. *Meteoritics & Planetary Science* 32:231–247.
- Rubin A. E. 2003. Chromite-plagioclase assemblages as a new shock indicator; Implications for the shock and thermal history of ordinary chondrites. *Geochimica et Cosmochimica Acta* 67:2695–2709.
- Ruzicka A., Snyder G. A., and Taylor L. A. 1998. Mega-chondrules and large, igneous-textured clasts in Julesberg (L3) and other ordinary chondrites: Vapor-fractionation, shock-melting, and chondrule formation. *Geochimica et Cosmochimica Acta* 62:1419–1442.
- Ruzicka A. M., Greenwood R. C., Armstrong K., Schepker K. L., and Franchi I. A. 2019. Petrology and oxygen isotopic composition of large igneous inclusions in ordinary chondrites: Early solar system igneous processes and oxygen reservoirs. *Geochimica et Cosmochimica Acta* 266:497–528.
- Snetsinger K. G. and Keil K. 1969. Ilmenite in ordinary chondrites. *American Mineralogist* 54:780–786.
- Spurný P., Borovička J., and Suchan P. 2017a. Meteorite Hradec Kralove found in the predicted area. Astronomical Institute AS CR. [https://www.astro.cz/clanky/slunec\\_nisoustava/meteorit-hradec-kralove-nalezen-v-predpovezene\\_oblasti.html](https://www.astro.cz/clanky/slunec_nisoustava/meteorit-hradec-kralove-nalezen-v-predpovezene_oblasti.html). Accessed February 11, 2020.
- Spurný P., Borovička J., Baumgarten G., Haack H., Heinlein D., and Sørensen A. N. 2017b. Atmospheric trajectory and heliocentric orbit of the Ejby meteorite fall in Denmark on February 6, 2016. *Planetary and Space Science* 143:192–198.
- Spurný P., Borovička J., and Shrubny L. 2020. The Žďár nad Sázavou meteorite fall: Fireball trajectory, photometry, dynamics, fragmentation, orbit, and meteorite recovery. *Meteoritics & Planetary Science* 55:376–401.
- Starkey N. A., Jackson C. R. M., Greenwood R. C., Parman S., Franchi I. A., Jackson M., Fitton J. G., Stuart F. M., Kurz M., and Larsen L. M. 2016. Triple oxygen isotopic composition of high- $^3\text{He}/^4\text{He}$  mantle. *Geochimica et Cosmochimica Acta* 176:227–238.
- Stöffler D., Keil K., and Scott E. R. D. 1991. Shock metamorphism of ordinary chondrites. *Geochimica et Cosmochimica Acta* 55:3845–3867.
- Tait A. W., Tomkins A. G., Godel B. M., Wilson S. A., and Hasalova P. 2014. Investigation of the H7 ordinary chondrite, Watson 012: Implications for recognition and classification of Type 7 meteorites. *Geochimica et Cosmochimica Acta* 134:175–196.
- Taricco C., Bhandari N., Cane D., Colombetti P., and Verma N. 2006. Galactic cosmic ray flux decline and periodicities in the interplanetary space during the last 3 centuries revealed by  $^{44}\text{Ti}$  in meteorites. *Journal of Geophysical Research* 111:A08102.

- Van Schmus W. R. and Wood J. 1967. A chemical-petrologic classification for the chondritic meteorites. *Geochimica et Cosmochimica Acta* 31:747–765.
- Wasson J. T. and Kallemeyn G. W. 1988. Compositions of chondrites. *Philosophical Transactions of the Royal Society of London* 325:535–544.
- Wlotzka F. 1993. A weathering scale for the ordinary chondrites (abstract). *Meteoritics* 28:460.
- Wlotzka F. 2005. Cr spinel and chromite as petrogenetic indicators in ordinary chondrites: Equilibration temperatures of petrologic types 3.7 to 6. *Meteoritics & Planetary Science* 40:1673–1702.
- Wlotzka F., Jull A. J. T., and Donahue D. J. 1995. Carbon-14 terrestrial ages of meteorites from Acfer, Algeria. LPI Technical Report #95-02. pp. 72–73.
- Xie X., Chen M., and Wang D. 2001. Shock-related mineralogical features and PT history of the Suizhou L6 chondrite. *European Journal of Mineralogy* 13:1177–1190.
- Zurfluh F. J., Hofmann B. A., Gnos E., Eggenberger U., and Jull A. J. T. 2016. Weathering of ordinary chondrites from Oman: Correlation of weathering parameters with  $^{14}\text{C}$  terrestrial ages and a refined weathering scale. *Meteoritics & Planetary Science* 51:1685–1700.

## SUPPORTING INFORMATION

Additional supporting information may be found in the online version of this article.

**Fig. S1.** Specimen 2 showing an incipient secondary fusion crust consistent with the fragmentation that occurred at a height of 30.7 km followed by exposure to heating during the last flight down to 21.5 km (Gardiol et al. 2021).

**Fig. S2.** Video, obtained with a high resolution structured-light 3-D scanner, showing the main mass (in the article referred as to specimen 2) of the Cavezzo meteorite.

**Fig. S3.** Pie-chart showing the modal mineralogy of specimen 1 and specimen 2. Metal and sulphides are not represented because  $<0.1\%$ .

**Fig. S4.** Cavezzo (specimen 1 and specimen 2): the average ferrosilite and fayalite contents, respectively of low-Ca pyroxene and olivine, plot within the expected values for type L ordinary chondrites.

**Fig. S5.** Low-Ca and high-Ca pyroxene composition of specimen 1 (pink) and specimen 2 (red). Two distinct groups of pyroxenes are clearly visible as well as the lack of pigeonite or augite. The compositions are in such a narrow field that many symbols are superimposed on each other.

**Fig. S6.** Feldspar composition of specimen 1 (cyan) and specimen 2 (blue). The composition, as can be seen clearly in this plot, is relatively homogeneous and many values overlap each other.

**Fig. S7.** Specimen 1 of the Cavezzo meteorite. Above: “achondritic” texture of the sample 1c dominated by large olivine crystals. Below: in this portion of the sample 1b, the chondrules are intermingled with large olivine crystals and a gradual transition to the “achondritic” portion of the specimen can be seen. Field width 10 mm.

**Fig. S8.** X-ray tomography showing the distribution of Fe,Ni metal and sulphides inside the Cavezzo main mass (specimen 2).